CATÓLICA
ESCOLA SUPERIOR DE BIOTECNOLOGIA

PORTO

Smart data driven predictive model application for wound healing tracking

by
Pedro Daniel Ribeiro Neto

May 2021

CATÓLICA
ESCOLA SUPERIOR DE BIOTECNOLOGIA

PORTO

Smart data driven predictive model application for wound healing tracking

Thesis presented to Escola Superior de Biotecnologia of the
Universidade Católica Portuguesa to fulfill the requirements of Master of Science degree in Biomedical Engineering

by
Pedro Daniel Ribeiro Neto

Supervisor: Prof. Doutor Pedro Miguel de Luís Rodrigues
Escola Superior de Biotecnologia, Universidade Católica Portuguesa

Co-Supervisor: Prof. Doutora Freni Kekhasharú Tavaria
Escola Superior de Biotecnologia, Universidade Católica Portuguesa

May 2021

Abstract

Chronic wounds affect millions of people around the world. Just in the United States, it is estimated that 6.5 million people suffered from chronic wounds, while in Europe the number is estimated to be around 1.5 to 2 million. The number of chronic wounds in Portugal isn't well known but at least 14,000 people suffer from leg ulcerations at any given time. Chronic wounds tend to affect people of older age or that suffer from chronic diseases such as diabetes. The increase of the average age of the populations in developed countries, coupled with the increase of diabetes cases will only exacerbate the problem of chronic wound prevalence. Despite all the wide array of innovative and potential treatments, current dressings do not provide any feedback information regarding the wound healing process. Developments in biosensors for wounds are being made, however, the processing of the gathered information is still lacking. Using the computational power of today's processors, a wound healing application was developed that was able to predict wound healing states, infected vs. non-infected, using only inexpensive sensors, thermal images, simple signal processing techniques, and features. Data was collected from 3D skin models and processed using Wavelet transform a powerful tool used in signal analysis allowing the decomposition of humidity and temperature signals in its frequency, even at the low sampling frequency. Features were collected from both humidity, temperature signal, and thermal images, and were selected through a process of feature selection and then feed to machine learning algorithms. It reached a maximum accuracy of 85.7% using a combination of temperature and humidity features feed to a logistic regression algorithm, as well as a Convolutional Neural Network, demonstrating the viability of this method.

Key words: Wound healing, Chronic Wounds, Machine Learning, Wavelet Transform

Resumo

As feridas crónicas afetam milhões de pessoas em todo o mundo. Alguns estudos estimam que as feridas cronicas afetam 6,5 milhões de pessoas nos Estados Unidos e 1,5 a 2 milhões de pessoas na Europa. Apesar de existirem poucos estudos sobre a prevalência de feridas crónicas em Portugal, é estimado que 14 mil doentes sofram de ulcerações crónicas na pele. As feridas crónicas tendem a afetar pessoas mais idosas ou que sofram de doenças crónicas, como por exemplo diabetes. Com o aumento da idade média das populações em países desenvolvidos, aliado ao aumento de casos de diabetes, o problema das feridas crónicas tenderá a agudizar-se. Apesar da ampla gama de tratamentos inovadores, os curativos atuais não fornecem qualquer *feedback* sobre o estado de cicatrização de feridas. O desenvolvimento de biossensores capazes de recolher informação de uma ferida apresenta-se como um grande passo para o fornecimento de *feedback* do estado das feridas crónicas. Utilizando a capacidade de processamento dos computadores atuais, foi desenvolvida uma aplicação capaz de prever estados de cicatrização de feridas, infetado versus não infetado, usando apenas sensores de baixo custo, imagens térmicas e técnicas de processamento de sinal. Os dados foram recolhidos a partir de modelos 3D de pele e processados através da transformada de Wavelet, uma poderosa ferramenta utilizada na análise de sinais, permitindo a decomposição de sinais de humidade e temperatura em várias bandas frequenciais, mesmo com baixa frequência de amostragem. Características recolhidas a partir de sinais de humidade, temperatura e imagens térmicas foram selecionadas a partir de um processo de seleção de características, sendo depois fornecidas às entradas de um algoritmo de *Machine Learning*. Alcançou-se uma precisão de 85,7% usando uma combinação de características de sinais de humidade e temperatura com um algoritmo de regressão logística e também com uma Rede Neuronal Convolucional, demonstrando a viabilidade deste método.

Palavras Chave: Cicatrização de feridas, Feridas Crónicas, Machine Learning, Transformada de Wavelet

Acknowledgments

To the Faculty of Biotechnology who provided with the opportunities and tools to develop this dissertation.

To Professors Freni Tavaria and Pedro Rodrigues whose guidance, knowledge and teachings provided me with the skills to develop this dissertation.

To my family who always supported me in my endeavours.

Pedro Daniel Ribeiro Neto

Outline

List of Figures

List of Tables

Abbreviations and Symbols

AI	Artificial Intelligence
ALI	Air Liquid Interface
ANNs	Artificial Neural Networks
CE	Cornified Cell Envelope
CNN	Convolutional Neural Networks
DA	Discriminant analysis
DSP	Digital Signal Processing
DWT	Discrete Wavelet Transform
ECG	Electrocardiography
EEG	Electroencephalography
EMG	Electromyography
FT	Full thickness
KNN	k-nearest neighbour
LDA	Linear discriminant analysis
LR	Logistic Regression
NCFS	Neighborhood component feature selection
POC	Point of care
QDA	Quadratic discriminant analysis
SB	*Stratum Basale*
SC	*Stratum Corneum*
SG	*stratum granulosum*
SP	*Stratum spinosum*
SFS	Sequential feature selection
SGD	Stochastic Gradient Descent
WT	Wavelet Transform

CHAPTER 1

Introduction

1.1 Motivation

Chronic wounds are considered a silent pandemic. Just in the United States, chronic wounds affected 6.5 million people at one point, while in Europe the number is estimated to be around 1.5 to 2 million [1, 2]. Studies have also found that in Portugal at least 14,000 suffer from leg ulcerations [3]. Patients with chronic wounds suffer from pain and decreased quality of life, in addition to extra financial costs from treatments and medication. As the healing process for chronic wounds can last from months to years, it has a big financial burden on the patient and the healthcare systems [4]. Despite various and innovative treatments regarding wound healing, the monitoring aspect of this process is still undeveloped. With the rise of new biosensors, a new avenue for wound healing monitoring rises. The timelier an intervention is in a wound, the better is its outcome. With that in mind, this work sets into developing an application using machine learning capable of predicting wound states', in this case, infected vs. non-infected using inexpensive humidity and temperature sensors, in conjugation with thermal images. Since data gathering from patients in real-time was not possible, 3D skin models were used to evaluate this work's premise.

1.2 Contribution of this work

The developed work showed that a multi-band analysis performed through discrete wavelet transform was a good way to extract relevant information from signal/images to predict wound healing states employing machine learning tools pre-trained for that purpose. Hence, in accordance with the results obtained, this technique demonstrates a relevant potential to assist health care providers in wound states assessment.

1.3 Dissertation Structure

The structure of the dissertation is as follows: Chapter one provides the motivation for this work. In chapter two the skin structure and function, the wound healing process, chronic wounds, microbiology of the skin, and skin models are presented. Chapter three follows up with the exploration of signals and the state of the art of some biosensors. In chapter four machine learning is explored, as well as, feature selection where different techniques are described. This chapter is followed by chapter five where the methodologies for this work are explained, such as the models, data collection, the pre-processing and processing, as well as the feature extraction, and finally, the results are presented and discussed. In the last chapter, the conclusions obtained during this work are described and future improvements to this work are indicated.

CHAPTER 2

Skin - Introduction

2.1 Skin

Skin is considered the biggest organ in the human body covering, in an adult on average, 1.75 m^2 and weighing 5 kg. One of the most important functions of the skin is to work as an effective barrier between the outside and interior environment of an organism, as well as to regulate the internal environment of the body (homeostasis), particularly the water content and body temperature. The skin also acts as an integral part of the innate immune system forming the first line of defense against infection, reducing the microbial adherence and invasion [5]. This is an important role since the skin harbors a diverse variety of microbial communities [6].

There are two main types of skin. Glabrous skin (non-hairy skin), found on the palms and soles, is characterized by the lack of hair follicles and sebaceous gland in the dermis but the presence of encapsulated sense organs, as well as, thicker layer of the epidermis, and hair-bearing skin that has both hair follicles and sebaceous glans but does lack encapsulated organs [7].

Structurally the skin is divided into three layers, from the inner to outermost: hypodermis, dermis, and epidermis (figure 2.1), each of which has a unique structure, composition, and function [8].

The hypodermis, also known as subcutaneous tissue, represents the deepest part of the skin. It plays an important role in thermoregulation, insulation, nutrient reservoir, and shock absorber. It is mainly comprised of adipocytes, large, rounded cells with a lipid-laden cytoplasm (triglycerides, fatty acids), arranged in primary and secondary lobules, separated by connective tissue [8].

The dermis is bounded externally by its junction with the epidermis and internally with the hypodermis. It provides nutrients to the epidermis and acts as a cushion against mechanical injury [7]. It is in the dermis where you can find the sensory and motor nerve endings, as well as, the hair follicles, sweat glands, sebaceous glands, lymphatic vases, and capillary vessels [6, 7]. It is partitioned

into two sub-layers, the papillary and the reticular dermis, although there isn't a sharp delineation between the layers. The deepest layer, the reticular region is characterized by having an irregular, dense conjunctive tissue and receives its names from the dense concentration of collagen, elastic and reticular fibers. The papillary region, the most superficial layer of the dermis, is composed of conjunctive areolar tissue, it gives the dermis its irregular surface, which strengths its connection with the epidermis [7]. Many cell types populate this area of the skin (fibroblasts, dermal dendrocytes, mast cells, and histiocytes) [9].

The outermost layer of the skin, the epidermis, is made up of multiple cells, the major cell being the keratinocyte, making between 90% to 95% of the total cells. Other cells such as melanocytes, Merkel cells, and Langerhans cells are also present [7, 8]. The epidermis is divided into 5 layers: the *stratum basale* (SB), or *germinativum* often referred to as the basal layer. It contains active keratinocytes and it is often described as one cell thick [7, 10]; *Stratum spinosum*(SP) another layer of the epidermis is composed of enlarged keratinocytes. On top of the SP, it rests the *stratum granulosum* (SG). In this layer, the cells flatten, losing their nuclei and their cytoplasm appears granular, *Stratum lucidum*, only present, in the thicker areas of the skin such as palms and soles, is situated on top of the SG [7, 10]; finally, the outermost layer, the *stratum corneum*(SC), consists of primarily dead, mature and enucleated keratinocytes, chemically crosslinked to fortify the barrier of the skin [11].

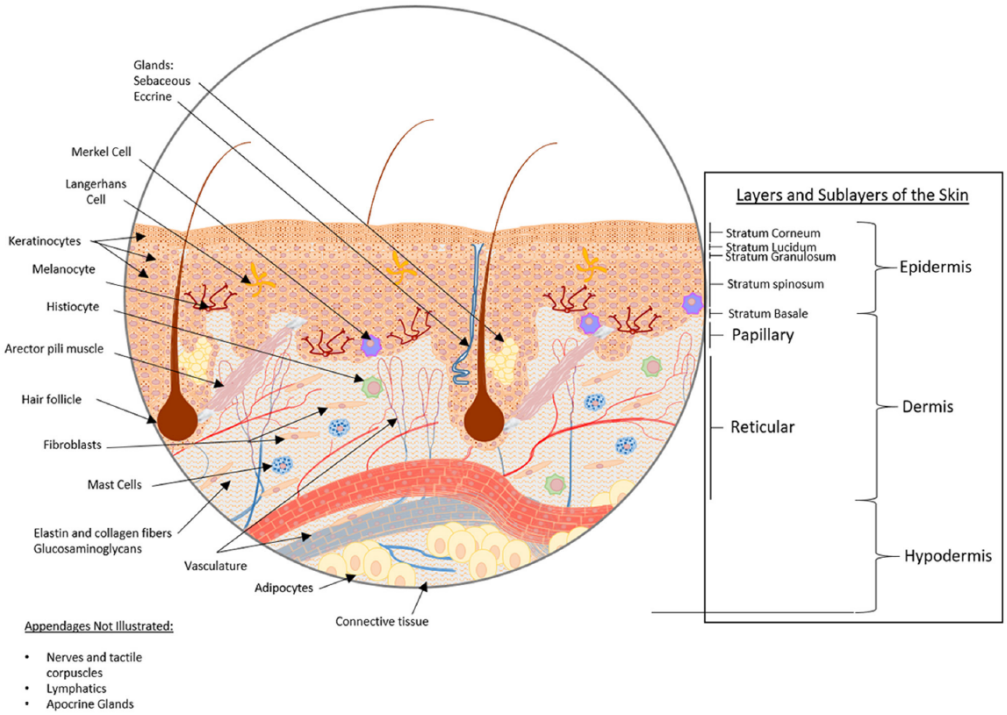

Figure 2.1: Healthy skin structure: layers, sublayers and appendages [9].

The main building blocks of the epidermis, keratinocytes are formed in the basal layer from epidermal stem cells [12]. This is the only layer where it is possible to find mitotically active cells. As the keratinocytes leave the basal layer and move upward to the skin surface, they withdraw from the cell cycle, switch off integrin expression, and start the differentiation program [13]. Making up a small part of the basal cell population, melanocytes produce the pigment melanin, which protects the keratinocytes from ultraviolet radiation [7]. As the cell moves upwards, the cells enlarge forming the stratum spinosum. A structure called a desmosome connects the cells, strengthening the bond between the cells. In this stratum, keratin starts being synthesized by the keratinocytes. The cells also release a water-repelling glycolipid, which prevents water loss, making the skin relatively waterproof. With the production of new keratinocytes in the stratum basale, the keratinocytes present in the stratum spinosum are pushed upwards into the stratum granulosum [14]. As they reach the stratum, the membrane thickens and large amounts of proteins, keratin and keratohyalin are synthesized. The nuclei and other cell organelles disintegrate as the cells die, leaving only behind keratin, keratohyalin, and cell membranes (corneocytes) that will form the stratum lucidum and stratum corneum. The stratum lucidum only present in the thick skin of the palms, soles, and digits, is located between the stratum granulosum and stratum corneum. The keratinocytes are densely packed with eleidin, a protein-rich in lipids, which provides a barrier to water [14].

The collapse of corneocytes into the flattened shape, which is characteristic of the stratum corneum layer, is made possible by the interactions between filaggrin and keratin, a fibrous structural protein found in vertebrates and a key structural material. Filaggrin, a matrix protein, aggregates the keratin filaments in a compact bundle. During this interaction, keratins are aligned into an order and condensed array. Between 80 to 90% of the protein mass of a mammalian epidermis is made up of keratins and filaggrin [15, 16]. Situated under the cytoplasmatic membrane and occupying the exterior of the corneocytes, the cornified cell envelope is a thought protein/lipid polymer. The connection of keratinocytes of the granular layer with the corneocytes is important for stratum corneum cohesion. This connection is possible thanks to desmosomes a cell structure specialized in cell-to-cell adhesion. The mechanical and chemical protection is provided by the corneocytes and in conjunction with intercellular lipid, it also confers water impermeability [16].

The skin is a continuously self-renewing organ. It is replaced by a process of desquamation, a complex biologic event [17]. Through the process of desquamation, the outermost layer of corneocytes is shed at a rate that balances the production of new corneocytes, to maintain the same thickness of the stratum corneum [18].

2.1.1 Skin Microbiome

The skin acts as an interface between the outside world and the human body. As such, it is colonized by a diverse collection of microorganisms like bacteria, fungi, viruses, and mites [19]. They play a role in the protection against the invasion of pathogenic or harmful microorganisms. They also

act as "teachers" to T cells that are found in the skin by teaching them how to respond to similar but more pathogenic cousins and play a role in the breakdown of natural products secreted by the skin [6, 19].

The skin lacks many nutrients beyond the basic proteins and lipids [6]. It is generally cool, acidic, and desiccated, but it has distinct habitats based on skin thickness, folds, and presence of hair follicles and sebaceous and sweat glands [6]. The skin sites can be divided into three more specific sites, based on their physiological characteristics, sebaceous (oily) areas (such as the face, chest, and back), moist areas (bend of the elbow, back of the knee, armpits, toe web, and groin) and dry areas (volar forearm and palm) [19]. The sebaceous gland is an appendage that is connected to the hair follicles that produces sebum, a substance rich in lipids. Besides protecting and lubricating the hair and skin, it also acts as an anti-bacterial shield [19]. These glands support the growth of facultative anaerobes such as *Propionibacterium acnes*, a common bacterium in the skin. These bacteria break down the triglycerides that make up part of the sebum, into free fatty acids. These acids contribute to the acidic pH (around 5) of the skin. Colonization by *Staphylococcus aureus* and *Streptococcus pyogenes*, common pathogens in the skin, are inhibited by acidic pH. Skin occlusion results in an elevated pH, which favors the growth of *S. aureus* and *S. pyogenes* [19]. *Staphylococcus* and *Corynebacterium spp.* are the most abundant organisms in the moist areas. These organisms use the urea present in the sweat as a nitrogen source. The processing of apocrine sweat results in the characteristic odor associated with it [19]. Dry areas tend to be more diverse, with *Actinobacteria*, *Firmicutes*, *Bacteroides*, and *Proteobacteria* all present, while sebaceous sites have the lowest diversity. These areas tend to be more stable over time when compared to dry ones [19]. Figure 2.2 demonstrates the distribution of bacteria in the skin.

It is widely accepted that culture-dependent approaches to assess the variety of microorganisms present in the human skin, reveals an incomplete picture. *Staphylococcus spp.* are more easily cultivated than *Propionibacterium spp.* or *Corynebacterium spp.* which were frequently underestimated in culture-based surveys [20]. With these methods, it was thought that *S. aureus* and *S. epidermidis* dominated the skin microbiota. However, with the use of 16S ribosomal RNA sequencing, it became evident that these species only represented 5% of the microorganisms present in the skin, while showing that sebaceous areas are dominated by *Propionibacterium* species. Bacteria that thrive in humid areas such as Staphylococcus and *Corynebacterium* species are abundant in moist areas. Dry areas have also a high concentration of *Propionibacterium acnes* and *Corynebacterium tuberculostearicum*, as well as a high diversity of Streptococcus species [10]. It is important to recognize the limitations of sequencing-based methods. While sequencing-based approaches do not require growth and isolation of microorganisms in culture, they aren't capable of distinguishing between live and dead microorganisms and are unable to show if a certain species was recently acquired or it is a stable microorganism of the skin, a transient member, or deceased. Skin specimens are typically low in bioburden and extremely susceptible to reagent and environmental contamination which might produce false-positive results. They also require reference databases that exclude uncharacterized microbes [6]. A mixed approach

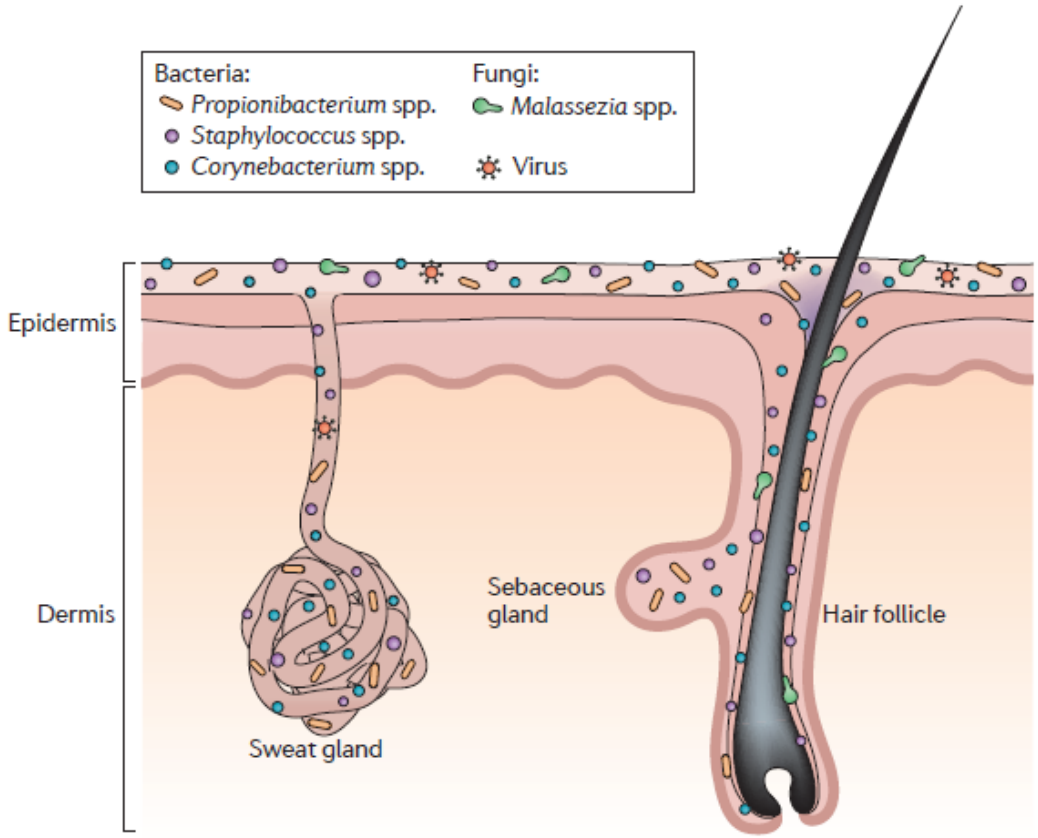

Figure 2.2: Spatial distribution of microorganisms in the skin [6].

of culture-dependent and independent methods can be made.

In an ideal world, samples for culturing should be processed immediately after collection. Depending on the objective, various media and growth conditions can be used to quantify the skin microbiota. For example, if the objective is the quantification of the most abundant microbial species in the skin, then separated specimens should be collected for aerobic and anaerobic growth. Once isolated, colonies can be identified using 16S rRNA gene sequencing. Since reagent contamination is a major problem, including culture-based methods allows assessing the plausibility of observing a given species in the skin [21].

2.2 Wound

The skin is continuously subject to various injuries and can be wounded physically or chemically. The complexity of skin injuries due to wounding and physical trauma is interdependent on the mode of wounding, followed by a series of complex events to repair and reestablish integrity and function [22]. Superficial partial-thickness wounds generally involve minimal structural damage, that can be healed

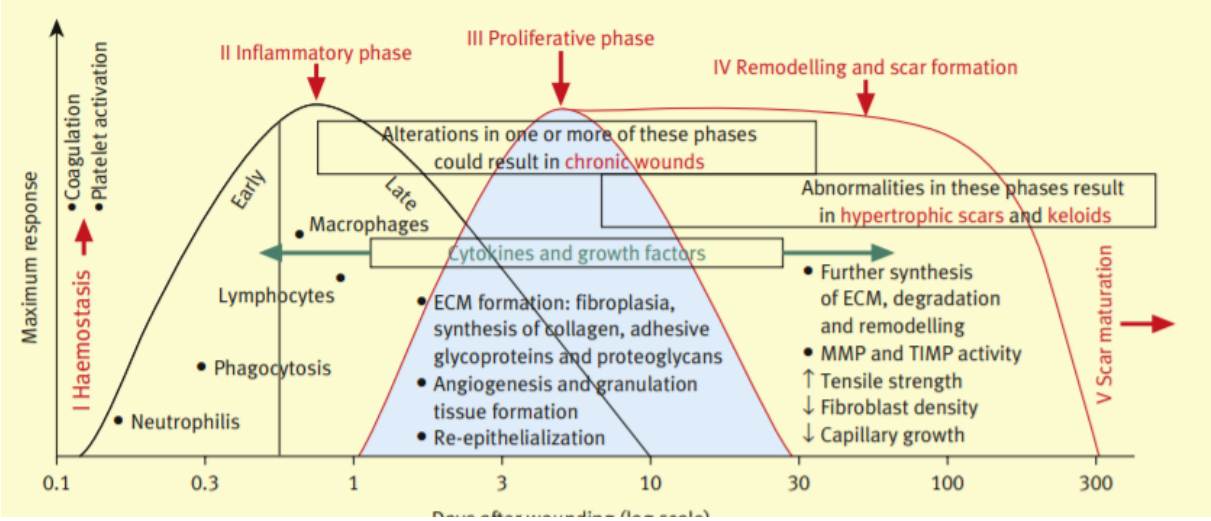

Figure 2.3: Wound healing phases over time [25].

within approximately two weeks. However, deep partial-thickness wounds that include damage to structural components such as blood vessels, nerves, and hair follicles take longer times. In particular critical cases, muscles and bones can also be damaged. Numerous studies have been performed to determine the wound healing process and identify compounds that promote wound healing and reduce scar formation [23]. Normally, the healing process proceeds through three distinctive major stages: inflammation (preceded by hemostasis), proliferation, and remodeling (Figure 2.3). Many factors can interfere with one or more phases of the healing process. There can be local factors such as the level of oxygenation, infections, or the presence of a foreign body or systemic factors like age, gender, stress, diseases, obesity, or nutrition. Local factors are those that directly influence the characteristics of a wound, while systemic factors affect the overall health of the individual which, in turn, affects its ability to heal. Many of these factors are related, and the systemic factors act through the local effects affecting the wound healing process [24].

2.2.1 Wound healing

2.2.1.1 Hemostasis

Hemostasis is the first stage in the wound healing process. The tissue injury leads to the disruption of blood vessels (most of the time) and the extravasation of blood constituents. The subendothelial collagen is exposed to platelets that will result in the aggregation of these components. It results in the activation of the intrinsic part of the coagulation. The contact between collagen and platelets, as well as the presence of thrombin and fibronectin results in the release of cytokines and growth factors. The clot serves as a scaffold for the cells such as neutrophils, monocytes, fibroblasts, and endothelial cells. It also acts by protecting from invading pathogens such as bacteria. Inadequate clot formation

(factor XIII - the fibrin-stabilizing factor) is associated with impaired wound healing, either because of decreased adhesion of cells into the inflammatory area or decreased chemotaxis [26].

2.2.1.2 Inflammation

The inflammation stage occurs next, starting with chemotaxis, the movement of an organism in response to a chemical stimulus. Somatic cells, bacteria, and other single-cell organisms direct their movement according to the presence of certain chemicals in their environment. Neutrophils are the first cells that migrate to the wound and have the function of cleaning the wound area from foreign particles and bacteria. The increased vascular permeability due to inflammation, the release of prostaglandins together with the concentration of gradients of chemotactic substances stimulate neutrophil migration. Selectins are receptors on the endothelial cell surface, that preferentially help neutrophils adhere to the endothelium. Integrin receptors on the neutrophil cell surface facilitate the binding to the extracellular matrix. Several factors stimulate both chemotaxis and proliferation, depending on the concentration of said factors. The chemotaxis of cells into the wound healing medium is followed by functional cell activation. Cell activation implies the phenotypic altering of cellular, biochemical, and functional properties that are induced by local mediators. All cells that participate in a successful wound healing process must be activated. Neutrophils, macrophages, and lymphocytes predominate during inflammation, but their contribution to the successful outcome of wound healing is variable. Macrophages and lymphocytes have critical roles in wound healing, but if there isn't a bacterial infection, the role of neutrophils is diminished. The activation of macrophages has a fundamental role in various wound healing aspects, such as debridement, matrix synthesis, and angiogenesis. The brief and initial release of factors from platelets is a strong stimulus to macrophage activation. Besides, the phagocytosis of cellular debris such as fibronectin and collagen also contribute to their activation. The activation of macrophages leads to the release of cytokines, which mediate angiogenesis (creation of new blood vessels) and fibroplasia. The activation of wound macrophages also results in the synthesis of nitric oxide, with many functions one being its antimicrobial properties. It was shown that in impaired wound healing there is inhibition of nitric oxide. Macrophages can also activate other cells such as lymphocytes via cytokines [27, 28].

The activation of cells during wound healing also means that there are profound phenotypic changes in certain cell populations. Fibroblasts and epidermal cells are some of the populations that can undergo this phenotypic change. The matrix that surrounds the cells also influences their phenotype. An example is the cell adhesion promoted by the synthesis of fibronectin (extracellular matrix molecules), which can result in phenotypic changes. A reduced inflammatory response profoundly affects subsequent healing, as demonstrated clinically and experimentally in diabetes and steroid treatment. In diabetes, besides the reduced activation of inflammatory cells coupled with diminished chemotaxis results in the less efficient elimination of bacteria which can result in bacterial infection and reduced collagen deposition [26].

2.2.1.3 Proliferation

At this stage, tissue formation occurs where fibroblast and endothelial cells are the primary cells that proliferate during this phase. The fibroblasts migrate into the wound site from the surrounding tissue while endothelial cells proliferate from intact venules close to the wound. Endothelial cells will form new capillaries by the process of angiogenesis. The growth factors and cytokines responsible for the proliferation derive mainly from platelets and activated macrophages. In excisional wound healing, epithelial cell proliferation is extremely important in reestablishing a barrier against fluid loss and infections. The proliferation of epithelial cells starts a few days after the wounding. The hotspots for the proliferation tend to be the wound edges or isolated areas in the middle of the wound with uninjured epithelial cells [26].

2.2.1.4 Remodeling

As the final stage of the healing process, tissue remodeling occurs; The main feature of the maturation phase is the deposition of collagen in the wound. From a clinical viewpoint, this is the most important phase because the rate, quality, and total amount of matrix deposition determine the strength of the scar. Many healing deficiencies become clinically manifest secondary to poor collagen deposition. In the case of diabetes, one of the reasons is reduced inflammatory response [26].

Deposition of the matrix in the wound, changes in the wound matrix composition follow a certain pattern over time. Initially, it is composed mainly of fibrin and fibronectin originating from hemostasis and macrophages. Thrombospondin1 is another early expressed protein that supports cellular recruitment in the wound milieu (medium). The healthy dermis is composed predominantly of collagen I (80% to 90%) and collagen III (10% to 20%), wherein granulation tissue, the percentage of collagen III increases to 30%. In mature scar tissue, the percentage of type III collagen is around 10% [27].

Net collagen synthesis is increased for at least 4 to 5 weeks after wounding. Fibroblasts are the main synthesizing cells. The structure of the matrix changes as well, normal dermis shows a basket weave-like pattern, whereas in the scar the thinner collagen fibers are arranged parallel to the skin. Along the stress lines of the wound, the thinner collagen fibers organize along those lines and thicken. With the thickening of the collagen fibers the tensile strength of the scar increases [29]. However, even with the long remodeling phase (up to 1 year), the collagen fibers in the healed scar tissue never become as organized as in the intact dermis. Because of that, the strength of the scarred tissue never reaches the same strength as it was before the wounding [26].

2.2.2 Chronic Wounds

The most common definition for chronic wounds has been defined as “ulcers (wounds) older than 3 months of age”. A more mechanistic definition such as wounds that don’t follow a normal wound

healing pathway has been proposed [30]. Chronic wounds are usually trapped in an uncoordinated and self-sustaining phase of inflammation [31]. Clinically, a wound can be categorized as acute or chronic based on the duration of the healing process, however, this is an arbitrary distinction, often based on different variables including the duration of the healing process, the cause and site of the wound, the age and physical condition of the patient [32]. The incidence of chronic wounds is especially high in the elderly and nursing-home populations, as well as, in people diagnosed with diabetes mellitus [30, 33]. Clinically chronic wounds are traditionally divided into various groups. Pressure, venous leg ulcers, and diabetic foot ulcers constitute approximately 70% of all chronic wounds [33]. Most chronic wounds are caused by a small number of conditions, such as arterial, and venous diseases, pressure sores, and Diabetes Mellitus [32].

Bedridden or post-operation patients are at higher risk of developing pressure ulcers [34]. This kind of ulcer is characterized by deep tissue necrosis. Although numerous factors contribute to the formation of a pressure ulcer, the key factor in the formation of this type of ulcer is the pressure over bony prominences. Other factors such as shear force, friction, and moisture are also important [33].

The exact cause for the formation of venous ulcers isn't certain, however, it occurs almost exclusively in association with chronic venous insufficiency [33]. It is the most common ulcer in the lower leg and is characterized by the presence of prolonged venous hypertension [30, 33].

Chronic foot ulcers or diabetic ulcers are the leading cause of foot amputation in diabetic patients [35]. Diabetic patients are at a 25% risk of developing a foot ulcer, during their life. Diabetic foot ulcers are the result of the simultaneous action of multiple contributing causes. Neuropathy and ischemia are noted to be the major underlying causes of foot ulcers [36]. Sixty percent or more of diabetic foot ulcers are the results of neuropathy [37]. The hyperosmolar hyperglycemic state results in an increase in the activity of the enzymes aldose reductase and sorbitol dehydrogenase. Intracellular glucose is converted into sorbitol and fructose. High concentrations of fructose results in a low level of synthesis of nerve cell myoinositol, necessary for the normal neuron conduction [36].

While a bacterial infection may not be the cause of an initial wound, microorganisms can contribute to the lack of healing [38]. Chronic leg ulcers are complicated by *Staphylococcus aureus* and *Pseudomonas aeruginosa*, present in 93.5% and 52.2% of evaluated ulcers [39]. In acute ulcers, *S. aureus* produces several virulence factors, such as, enterotoxins, toxins, hemolysins, metalloprotease, and hyaluronidase, that are inactivated by the immune system, and bacterial are destroyed by neutrophils. In chronic wounds *S. aureus* and *P. aeruginosa* plays a central role as they tend to be the first pathogens found. There is an increased expression of virulence factors leading to severe infection and antibiotic resistance [40]. These pathogens, common on chronic wounds, are also typical biofilms producers. Bacteria that reside within biofilms are highly resistant to many traditional therapies, with reports showing that bacteria within biofilms are up to 500 times more resistant to antibiotics [41].

2.3 Abiotic factors prevailing the skin

The effects of abiotic factors such as pH, fat, sweat, and temperature in the skin microbiota were previously discussed. However, these factors may also affect the barrier function of the skin surface and wound healing.

The acidic nature of the skin has long been described by Heuss [42]. Various studies have shown this acidic nature of the skin with pH values as low as 4.0 and up to 6.3. The age of a person has been shown to influence the skin pH. A study by *Visscher et al.* [43] reported a relatively neutral surface pH in neonates with a decrease to about 5.5 in the first 3 days. This is corroborated by a study by *Yosipovitch et al.* [44] where initial values of 7.08 were reported followed by significant decreases in the pH by the second day of life.

The enzymatic activity is also altered by the pH levels. Serine proteases, kallikrein 5 (SC tryptic enzyme), and kallikrein 7 (SC chymotryptic enzyme) have neutral optima and are linked to the desquamation process. As the pH increase, these proteases are activated, while enzymes responsible for generating ceramides which have acidic optima are inactivated, therefore compromising the SC structure and function [45]. As, the enzymatic activity, skin pH also was shown to influence the skin microbiota and the wound healing process. The bacteria *Propionibacterium acnes* capable of breaking down the triglycerides present in the sebum is widely accepted by dermatologists to be associated with the development of acne. While new studies have shown that the presence of this bacteria in healthy and acne patients is similar, specific strains of *P. acnes* may cause the development of acnes [46]. *P. acnes* multiply well in pH values between 6 and 6.5 but in values below 6 its growth decreases [45]. A study comparing the number of inflammatory lesions in acne-prone patients using conventional alkaline soap versus an acidic syndet bar showed that the number of inflammatory lesions increased with the alkaline soap and decreased with the acidic one [47]. *Staphylococcus aureus* a pathogen commonly found in skin infections and chronic wounds has its growth strongly surpassed at acidic pH levels, while it thrives in neutral pH [31]. Correlations between the evolution of wound into an acute or chronic wound, as well as, and wound infection have been drawn [48]. *Roberts et al.* (1997) [49] showed that wounds with a high pH had a lower healing rate when compared with wounds with a pH closer to neutral. Work by Hoffman also showed that in alkaline conditions, wound healing rate decreased [50]. Another study by *Shuka et al.* (2007) which assessed the relationship between wound pH and the state of a wound showed that at a baseline, the pH of the majority of the wounds was greater than 8.5, yet as the wounds showed signs of healing it reduced to values lower than 8.0 [51].

The effects of temperature in wound healing have long been recognized. Primarily determined by the ambient temperature and blood flow, the temperature in acute wounds increases due to local vasodilation, allowing the body to deliver more oxygen and nutrients to the injured area, resulting in higher metabolic rates. Comparatively in most chronic wounds, the temperature is approximately 5ºC lower than the core temperature [52]. The relationship between the absolute temperature of the wound and the temperature of the wound relative to the adjacent intact skin has been described.

An acute wound that heals spontaneously is warmer than 37ºC, but not significantly warmer than the peri-wound area. In chronic wounds, the temperature is approximately 5ºC lower than the core temperature due to the impaired blood supply and oxygenation [53]. A study by *Denda et al.* (2007) also showed that temperature affects epidermal permeability and barrier function. In this study, the barrier recovery of both mouse and human skin was accelerated at a temperature between 36 and 40ºC, where at 34 or 42ºC it was delayed [54]. Low humidity had negative effects on the skin barrier function. Human skin exposed to low relative humidity levels, around 32%, appear to be more susceptible to mechanical stress and fracture of the skin than in high relative humidity levels (96%). In a study where healthy individuals were transferred from humid to dry conditions, a reduction in skin elasticity was observed. In another study factory workers under ultra-dry conditions (1 to 3% humidity), reported significantly more skin problems such as itching, contact, and atopic dermatitis [55]. Thanks to its low permeability, skin acts as a barrier preventing fluid loss, however, after an injury, disruption of the skin barrier leads to an increase in the loss of water vapor, as well as loss of electrolytes and fluids. Evaporation consumes energy, causing a loss of calories, and a decrease in the wound temperature [53]. A moist or wet environment improves the speed and quality of skin cicatrisation. A study by *Hackl et al.* (2012) demonstrated that a wet or a moist environment improved reepithelialisation in wounds [56].

2.4 Skin Models

The development of the first methods that describe the separation of human skin (epidermis from the dermis) and the isolation and culturing of human keratinocytes, occurred in the early fifties. Cultivation of adult mammalian skin epithelium *in vitro* was described for the first time in 1948. To study cell-cell interactions, regulation of proliferation and differentiation, wound healing, skin barrier function, and skin microbiome interactions, skin models better resemble the natural architecture and functions of the skin and should be considered as the gold standard when performing *in vitro* studies on human skin [57]. The reduced availability of human skin and the ethical issues related to animal experimentation empower the need and development of skin models, mimicking reality as closely as possible so that the drawn, results and conclusions are reliable. A huge milestone was achieved by Rheinwald and Green in 1975 who lethally irradiated 3T3 fibroblasts as feeder layers to generate a culture of human keratinocyte colonies that originated from a single keratinocyte. This discovery allowed scientists in the field of dermatology to generate large quantities of keratinocytes for *in vitro* cell culture studies and paved the way for the treatment of burned patients [58]. In fact, the complexity of the skin is often simplified when models are created, once its proper functioning depends on all the layers, cells, and appendages [8]. Since the beginning of the development of these models, it became possible to anticipate considerable evolution which will lead, in the future, to *in vivo* cultures really identical to the complex organ that skin is.

The first skin models were made in two-dimensional cell culture, where a monolayer of cells grew on a flat surface of glass or polystyrene, normally a petri dish. These cells were supplied with a nutritional medium with essential nutrients, such as vitamins, amino acids, minerals, and carbohydrates; growth factors, hormones; gases, as O2 and CO2, and it also regulates the physical-chemical environment (pH, osmotic pressure, and temperature) [59]. As this type of cell culture is monolayered one of the most important aspects is missed, the interaction between cells, which is much smaller than what actually happens in skin environments. Rheinwald and Green (1975) were also the first to describe that such monolayer culture can differentiate and form multilayered structures. Simplicity, high throughput, and reproducibility are major advantages of monolayered keratinocytes. However, many features of a fully stratified epidermis are lacking in this model, and keratinocytes are forced to adapt to artificial circumstances, like a flat surface and submerged culture, which may alter gene expression and cell structure [57]. With this set of limitations, in the modern age, it was crucial to develop 3D skin models and improve their resemblance with the actual environment and conditions of the skin.

2.4.1 The Phenion® Henkel Full-thickness 3D skin model

Constructed on the basis of a proprietary bovine collagen scaffold this model features morphological equivalence with human skin and allows convenient handling in research applications. The skin model production lab is located at the Biological and Clinical Research (BCR) Department within Henkel Beauty Care Technologies in Dusseldorf, Germany. It consists of human primary fibroblasts and keratinocytes from a single donor origin and the cell batches are carefully selected for optimal 3D-tissue composition. It has a cornified surface, a multi-layered epidermis, and the matured dermis displays an excellent elastic fiber network. Keratinocyte differentiation into a multi-layered stratified epithelium is associated with the expression of specific markers like cytokeratin 10, filaggrin, and transglutaminase. At the dermal-epidermal junction zone crucial basement membrane proteins, like collagen IV and VII and laminin-5 support epithelial adhesion. In the dermis, there are also established, during maturation, pivotal connective tissue components including collagenous and elastic networks (elastin and fibrillin-1). The model is a circular tissue with a diameter of 3 cm and, this type of tissue has long-term cultivation for at least 10 days which allows repeated treatments. The Phenion® Full-thickness apart from wound healing could also be used in the investigation of areas like cytotoxicity, skin metabolism, and genotoxicity [60].

CHAPTER 3

Instrumentation and Signal (1D and 2D)

Sensors react to a physical or chemical stimulus converting it into an electrical signal. As a significant number of biochemical processes are linked to the wound healing process, biomedical sensors can have an impact on the wound healing process as well as on infection prevention by monitoring the state of the wounds [61]. The use of thermal imaging can also be used for wound management [62]. This chapter will discuss signals, thermal imaging, and advancements in wearable biosensors for wound management and monitoring.

3.1 Signals

A signal can be defined as a function that conveys information about a system behaviour of a system or attributes of some phenomenon. We should consider acoustics waves that convey speech or music information and a hygrometer used for measuring water vapor in the air, soil, or confined spaces. A signal is not necessarily an electrical quantity. However, to perform activities such as recording, analyzing, and modifying signals, it is often convenient to use signals in the form of an electrical quantity [63]. As such, we can define a signal as a quantity measured over time.

Biosignals represent some aspect of a biological event. In their nature, they can be either deterministic signals often compact, described by syntactic techniques, or random signals which are mainly described by statistical techniques [64]. Biosignals can be divided into several groups based on their type of energy [65]. Neural cells use the depolarization of the cell membrane to transmit information throughout the body. These changes are recorded by surface electrodes that capture bioelectrical signals of groups of correlated nerve or muscle cells or by intracellular electrodes that record electric potential across an individual cell. These biosignals are commonly measured in Electrocardiography (ECG), Electroencephalography (EEG), and Electromyography (EMG) [64]. Variations on the pH level, O2 concentration, quantity of vapor water, or presence of a chemical

compound such as ammonia, can be captured and through signal processing can be used to determine or predicted a state of a wound. These biochemical signals can give us important insight to wound healing monitoring. The body organs also produce weak magnetic fields, and these biomagnetic signals can be used to produce three-dimensional images [64].

3.2 Thermal Imaging

Thermoregulation is one of the many functions of the skin. Because this thermoregulation responses to an internal or external stimulus, it has been used as a diagnostic aid since skin impairments often indicate health issues. Methods such as infrared thermal imaging have been explored for new applications in the medical field [66].

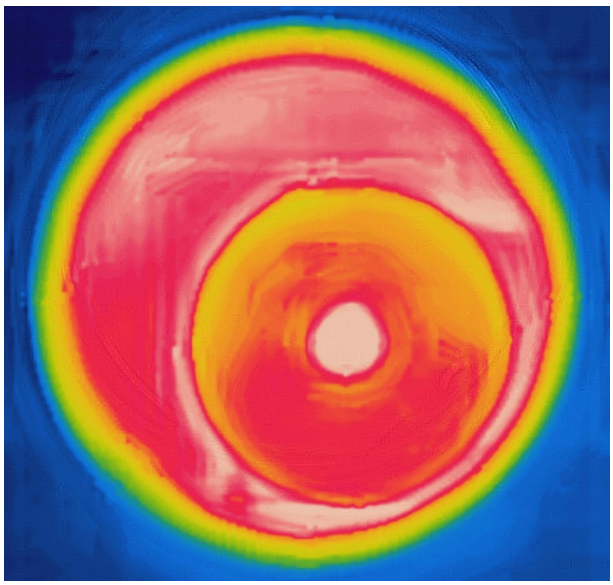

Figure 3.1: Example of a thermal image taken from a skin model.

According to Planck's law, every physical body spontaneously and continuously emits electromagnetic radiation at a given temperature. A body with a temperature superior to 0K emits infrared radiation, with the amount of radiation emitted increasing with temperature [67]. Thermographic cameras detect radiation in the infrared range of the electromagnetic spectrum (Figure 3.1). Studies were performed using thermal imaging to assess skin temperature following cryotherapy, as a safe and non-invasive method. It concluded that thermal imaging appeared to be an accurate and reliable method [68]. Thermal imaging utilization in diabetic foot diseased prevention and management can be beneficial. In a study carried by *Netten et al.* a high-resolution infrared camera algorithm for detecting diabetic foot disease signs and also discriminate between diabetic foot complications was created [69].

3.3 Biosensors for wound healing monitoring

The use of biosensors plays an important role in software that is based on monitoring the wound healing process. Chronic and acute wounds have a crucial impact on a patient's life quality. As a significant amount biochemical processes are linked to the wound healing process, biomedical sensors can have an impact on the wound healing process as well as infections prevention by monitoring the state of wounds [61].

The sensor's role is to provide some type of data at a defined point over time. However, this type of information only becomes valuable when it's linked to the state of a wound. As previously mentioned, the role sensors' role is to provide some data at a defined point over time, but this type of information only becomes valuable when it's linked to the state of a wound. As a result, the provided data can then be used for further monitoring of the wound healing process [70].

The biosensors for wound healing are supposed to have a biocompatible design. Additionally, be able to assure a free fluid flow, be stretchable and flexible. Consequently, it is important to combine the sensors with a substrate material that can fulfill these and further specific properties [71]. Since the sensors are supposed to be integrated into the dressings during the monitoring process, it is advised to use flexible biosensors. These biosensors could then be coupled with the notable detection biomarkers. Furthermore, these markers would be able to provide the user with continuous data about the wound status. However, to do so, a point of care (POC) system is required [72].

Devices that are based on POC services serve the purpose of providing medical assessment near or at the site of patient care. Due to their ability to turn around rapidly, the high level of convenience, and the ease of use based on the design, we can conclude that these technologies are ideal for wound management. With wound healing, POC technology appears to have a promising future. Based on the fact that relevant biochemical data can be processed without delay, optimal monitoring of the wound healing process may be guaranteed [70].

Table 3.1 and 3.2 summarizes the most common and promising markers for monitoring wound healing. Some current studies have focused on developing sensors that can detect bacterial colonization [72].

Table 3.1: Common physical biomarkers evaluated by biosensors for wound monitoring.

Physical Marker	**Indicator of**	**Normal values**	**Illness values**	**Main mechanism of measurement**
Temperature [52]	Inflammation, metabolic activity	31.1–35.4 ºC of skin	1.11 ºC increase at wound	Thermometer, thermogram, thermistor
Blood Pressure [72]	Hypertension	<115 mmHg systolic <80 mmHg diastolic	>115 mmHg systolic >80 mmHg diastolic	Strain gauge

Table 3.2: Common chemical biomarkers evaluated by biosensors for wound monitoring.

Chemical marker	**Indicator of**	**Normal values**	**Illness values**	**Main mechanism of measurement**
Glucose [73]	Insulin deficiency, diabetes melitus	3.9-7.8 mM in blood	>7.8 mM in blood	Chronoamperometry, absorptiometry
IL-6 [74]	Inflammation, elevated metalloproteinases	0 pg/μg on skin 0-2.4 pg/ml in blood	1.27 $\pm$ 1.7 pg/μg at wound >2.4 pg/ml in blood	ELISA, western blot
Lactate [75]	Hepatic disease, tissue hypoxia, hemorrhage, sepsis	0.5-1.5 mM in blood 1.0-3 mM on skin	>1.5 mM in blood >7 mM at wound	Chronoamperometry
pH [76]	Infection, acidosis, enzyme degradation rate, collagen deposition, fibroblast activity	4-7 pH of skin	7.15 - 8.90 pH at wound	Chronoamperometry, Optical transitions
Oxygen [77]	Metabolic activity, apoptosis, carbon monoxide	30-50 mmHg pO2 on skin 50-130 uL in blood 97% hemoglobin binding	5-20 mmHg pO2 in exudate 50-130 uL in blood <97% hemoglobin binding	Fluorescent sensing, clark-type electrochemical cell
Humidity [78]	Reepithelialization rate	4-8 g/m^2	100 g/m^2	Sweat rate gradient

3.3.1 Wound healing predictive models state of art

Other studies were published where colour and thermal images, in conjunction with machine learning techniques were used to try and classify based on different types of wounds. Table 3.3 summarizes the classification type, machine learning method used, and accuracy achieved. These works try to differentiate from different wound states, be it, infections, burns, or other abnormal classes.

The approach developed takes advantage of thermal cameras, as well as, temperature and humidity sensors.

Table 3.3: State of the art studies

Classification Type	**Machine Learning Method**	**Accuracy (%)**
Binary classification of infected and non-infected wound [79]	SVM	84.7
Three types of burn: superficial dermal, deep dermal, and full-thickness burn [80]	SVM	82.7
Three types of burn: superficial dermal, deep dermal, and full--thickness burn [81]	KNN	83.8
Binary classification of normal and abnormal classes [82]	CNN	90.7

CHAPTER 4

Machine Learning, Deep Learning and Feature Selection

This is the age of "big data". With the spread of personal computers, smartphones, and wireless communication, humans became big data producers. Every time a person searches for a website buys something online or post on social media is generating data. But it is also a data consumer. People want specialized services and products specially tailored to them. Algorithms were developed that connect a person's searches online and the ads that are targeted to them. However, some problems are so complex that these algorithms aren't enough. It can be more effective to let a machine develop its algorithm. Artificial Intelligence (AI) using Machine learning tools can be used to solve this kind of problem, as well as, having other applications such as email filtering and computer vision [83]. In this chapter machine learning and different algorithms will be discussed, additionally, it will also dive into deep learning a sub-class of machine learning, and convolutional neural networks (CNN) an application of DP. Feature selection and cross-validation will also be discussed.

4.1 Machine Learning

Machine learning is the programming of a computer model to perform and categorize based on sample data known as training data. By having a model defined by some parameters, learning is the execution of a program to optimize the parameters based on the training data. The model may be predictive meaning it can make predictions in the future, or descriptive meaning it gains knowledge from the data, or a mixture of both [83]. Traditionally there are three approaches to machine learning, based on the type of data in the input and output, and the type of task or problem it is trying to solve.

- **Supervised learning:** In this approach, the data set has both the input and the desired outputs. The training data consists of a set of training examples, with each example having desired

output labeled. In a mathematical model, each training example is represented by a vector, also known as a feature vector with each value representing a feature. The training data is represented by a matrix and the outputs by a vector. In cases of classification algorithms, the outputs are restricted to a limited set of values, while regression algorithms may have any numerical value within a determined range [83].

- **Unsupervised learning:** This approach is used to look for undetected patterns in a data set. There aren't any pre-existing labels, unsupervised learning algorithms take a data set only containing inputs and find structure in the data. Because these algorithms learn from training data that isn't labeled, classified, or categorized, they identify commonalities in the data. Besides finding previously undetected patterns, it is also used for feature learning [84].

- **Reinforcement learning:** In reinforcement learning, a program interacts with a dynamic environment. It must perform a certain action, which is interpreted into a reward and a representation of the state, which are feedback into the agent of the action [85].

4.1.1 Traditional Machine Learning Algorithms

4.1.1.1 Decision Trees

Decision trees are a type of supervised machine learning that uses a flowchart-like structure to go from observations of an object, represented as branches, to conclusions about the said object, represented in a node [83], as shown in figure 4.1. Starting in the initial node, it asks a question about a feature of the object and only has "yes" or "no" answers. For each of the answers, it is created a new child node. In this node, another question is asked about a different feature of the object, resulting in new child nodes.

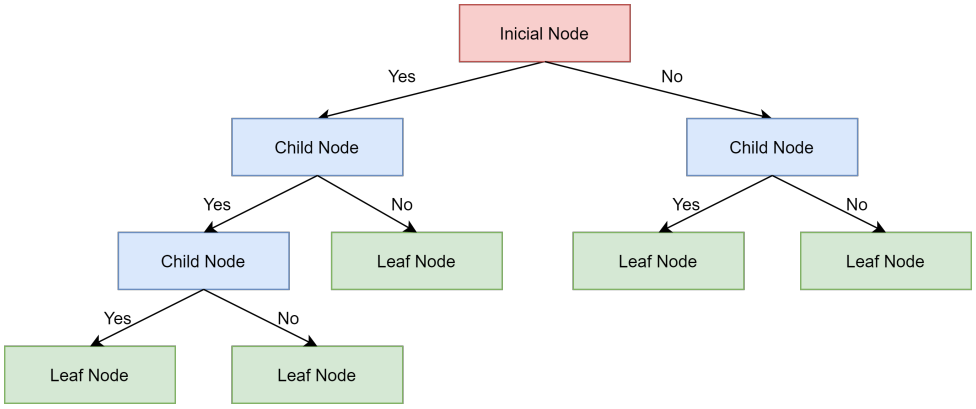

Figure 4.1: Example of decision tree classification.

This process repeats itself until it reaches a node without a child node, dominated by a leaf where a class is attributed to the object. A more simplistic view of the process is having an initial object, different questions are asked about the object until it is sorted into a class. In some variations, each leaf contains the probability of the object belonging to the class [86].

4.1.1.2 k-Nearest Neighbours

k-Nearest Neighbour (kNN) is an instance-based learning statistical method and used in supervised machine learning. They are designated lazy-learning algorithms, as they delay the induction or generalization process until the classification process. They require less computation time during the training phase, but more computation time during the classification process [87].

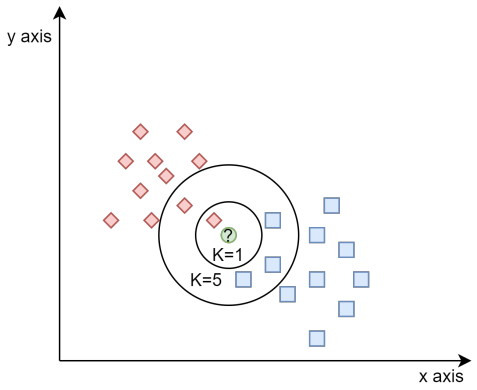

Figure 4.2: Example of KNN classification.

Generally, examples within a dataset will exist in proximity of others examples with similar features. Using this principle, examples are tagged through the training process and are then classified by calculating the distances to the nearest neighbours. With k=1, the simplest form of a kNN algorithm, an example will be classified based on its closest neighbour. With k>1, it locates the k nearest neighbours and classifies it based on the majority of neighbours close to the example (Figure 4.2). The distance between one example and its neighbours can be calculated based on Euclidean distance (equation 4.1), Cubic distance (equation 4.2) , Cosine Distance (equation 4.3) and Weight distance (equation 4.4) [87, 88],

$$D(x,y) = \sqrt{\sum_{i=1}^{n} (x_i - y_i)^2} \tag{4.1}$$

$$D(x,y) = \sqrt{\sum_{i=1}^{n} |x_i - y_i|^3} \tag{4.2}$$

$$D(x,y) = \frac{\sum_{i=1}^{n} x_i y_i}{\sqrt{\sum_{i=1}^{n} {x_i}^2}\sqrt{\sum_{i=1}^{n} {y_i}^2}} \tag{4.3}$$

$$D(x,y) = \sqrt{\sum_{i=1}^{n} w_i (x_i - y_i)^2} \tag{4.4}$$

where x and y represent two points in a Euclidean n-space, x_i and y_i and w_i the vector weights.

4.1.1.3 Discriminant Analysis

Discriminant Analysis (DA) is a supervised machine learning approach with the main goal of representing the matrix training data onto a lower-dimensional space while being able to separate into different classes. There are three main steps needed to achieve this reduction of dimensionality. The first step is to calculate the between-class variance, that is the distance between the means of different classes. This distance represents the separability between different classes. The following step is to calculate the within-class variation which is the distance between the mean and the examples of each class. The last step is the construction of the lower dimensional space that maximized the between-class variance and minimizes the within-class variance [89]. Linear Discriminant Analysis (LDA) and Quadratic Discriminant Analysis (QDA) are two types of DA, where the LDA obtains linear boundaries, where straight hyperplane divides the variable space into regions and allows discriminations between different classes with normal distributions (figure 4.3. QDA uses quadratic boundaries where a quadratic curve separates the class regions and allows different class-specific covariance for each class [90].

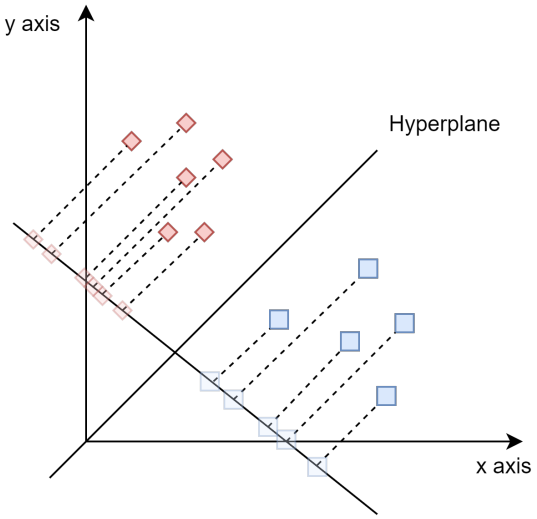

Figure 4.3: Example of LDA classification.

4.1.1.4 Logistic Regression

Logistic regression (LR) is a binary classification method used on supervised machine learning. It calculates the probability of an example belonging to one of two classes based on one or more independent variables using a logistic curve. The probabilities given are between 0 and 1. The probability of a given example belonging to 1 ($P(1|x,\alpha)$) is given by the equation 4.5 ,while the probability of belonging to 0 ($P(0|x,\alpha)$) is given by the equation 4.6.

$$P(1|x,\alpha) = \frac{1}{1+e^{-(\alpha * x)}} \tag{4.5}$$

$$P(0|x,\alpha) = 1 - P(1|x,\alpha) \tag{4.6}$$

A hyperplane is also drawn resulting in the decision boundary between the two classes since logistic regression only gives one example belonging to a class [91].

4.1.1.5 Support Vector Machine

A Support Vector Machine (SVM) is another type of supervised learning model. It is inherently a binary classification, the same as LR. Having a set of training examples each marked with one of two possible categories, an SVM training algorithm builds a model that will assign new examples to one of the two categories. In this type of model, each training example is represented as a point in space, mapped so that the examples belonging to each category are divided by a clear gap. Having the training examples mapped, a line denominated hyperplane is drawn between both groups' examples in order to maximize the separation between the two groups. It is this hyperplane function that will determine the class of a new example when being classified. Two parallel vectors used to build the hyperplane are also drawn and they are limited by the number of samples from both groups that are the closest to the hyperplane vector, with the distance between the two vectors refereed as the margin (Figure 4.4) [92, 93].

There are cases where it isn't possible to draw a hyperplane with a linear kernel (Equation 4.7) that separates both groups efficiently. In these cases, different kernel functions such as Polynomial kernel (equation 4.8) and Gaussian kernel (equation 4.9) can be used, where they transform the dimensional space in another of higher dimension [92, 93],

$$K(x_i, y_i) = x_i^T y_i + C \tag{4.7}$$

$$K(x_i, y_i) = (\gamma x_i^T y_i + r)^d, \gamma > 0 \tag{4.8}$$

$$K(x_i, y_i) = e^{-\gamma * ||x_i y_i||^2}, \gamma > 0 \tag{4.9}$$

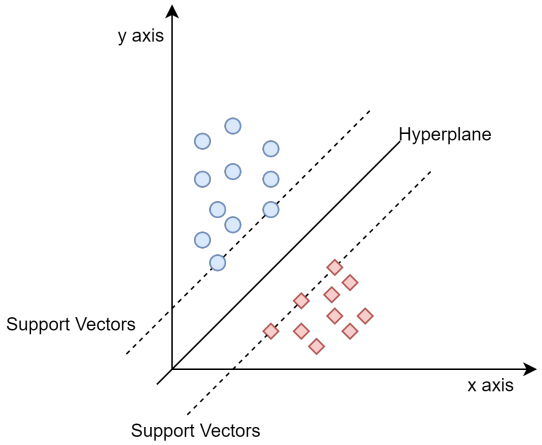

Figure 4.4: Example of Linear SVM classification.

where d is the polynomial order.

4.1.2 Deep Learning

4.1.2.1 Artificial Neural Networks

Artificial neural networks (ANNs) are a computational model inspired by the neurons that constitute an animal brain. The neurons in the brain receive signals through the synapses that are connected to the dendrites. When the transmitted signal surpasses a certain threshold, the neuron is activated and sends a signal through the axon. This signal may be sent to another neuron and activate. In ANNs an artificial neuron receives a signal (input), processes it, and transmits it to the connected neurons. The output signal results in the computation of the sum of input signals by some nonlinear function. Each input in the artificial neuron has a weight that is adjusted in the learning process. This weight increases or decreases the strength of the input signal at the connection. Similar to natural neurons, artificial neurons have a threshold where only the signal is transmitted only if the weighted sum of the inputs signals surpass the threshold [94].

The training process visualization is rather simple. In AANs there are usually three layers with its included neurons. The first layer represents the inputs while the second layer dominated the hidden layer, as shown by the figure 4.5. The neurons in the hidden layer take the sum of weight inputs and transform it based on a function resulting in an output. The resulting signal is then transmitted to the third layer, the designated output layer. It is in the neurons of this output layer where overall outputs are gathered [95].

Deep learning is part of the machine learning broader family that includes ANNs. CNNs, deep neural networks, deep belief networks, and recurrent neural networks are other architectures belonging to deep learning. The biggest difference between ANNs and Deep learning architectures is the number

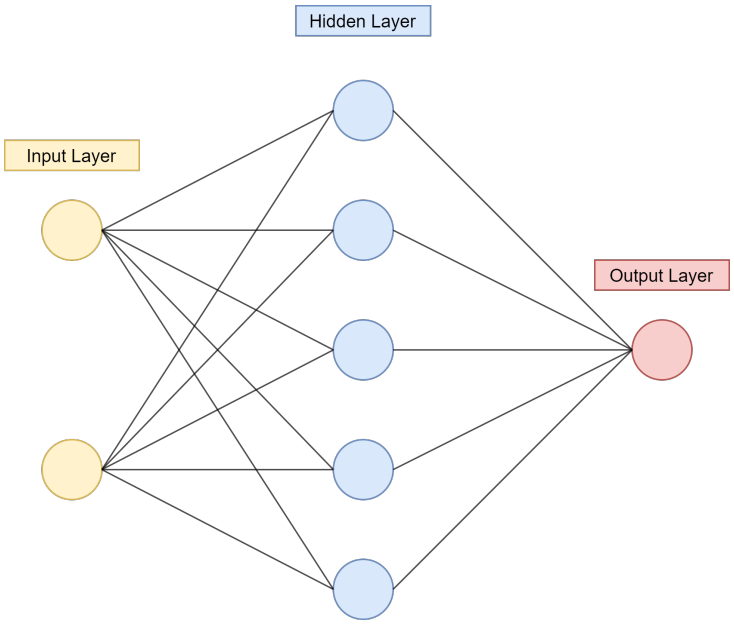

Figure 4.5: ANN classification example.

of hidden layers, their connections, and their capability to learn important abstractions of the inputs. ANNs are usually limited to three layers and are optimized for only one task. In comparison in every layer of a deep learning method, it results in a representation of the observed patterns based on the inputs from previous layers. In deep learning, these feature layers aren't designed by humans but are learned from the original data. These representations are then fed to a supervised layer that fine-tunes the network [96].

4.1.2.2 Convolutional Neural Networks

CNNs are a class of deep neural networks that are commonly applied in imaging and pattern classification. Over the years it has been used in speech emotion recognition and arrhythmia detection using ECG signals [95, 96]. It is multilayer perception meaning it uses a nonlinear instead of the linear activation function. It learns in a supervised manner, with some structural constraints. The first constrain featuring extraction results in each neuron taking its input from a local receptive field in the previous layer, extracting local features. The second constrain is feature mapping. Each layer of the network is composed of multiple feature maps with each neuron present in the layer share the same set of weights. The third constrain subsampling, means each convolutional layer is followed by a computational layer that performs local averaging and subsampling, resulting in the resolution of a given feature map being reduced [97].

There are different types of layers in CNNs. Convolutional layers are important to CNNs since even for a small image a very high number of neurons would be necessary to learn features. A

convolutional layer has a height and weight smaller than the input volume. Each filter is slide across the input and the dot products of the input and filter are computed at every spatial position. The output is obtained by stacking the activation maps of all filters along with the depth of each spatial position obtained [98]. Rectified linear unit (ReLU) layer typically follows a convolutional layer. It applies a non-saturating function activation function and effectively removes negative values from the feature maps by setting them at zero. In fully connected layers the neurons are connected to all neurons in the next layer. It is in this layer where the features obtained in the convolutional layer are interpreted and perform the function of high-level reasoning. The final layer of a CNN can often be a softmax layer. In this layer, a vector is taken of real numbers and normalizes into a probability distribution. It is used to predict if an object belongs to a determined class [99]. In figure 4.6 it is possible to see the visual representation of the CNN classification algorithm used in this dissertation work.

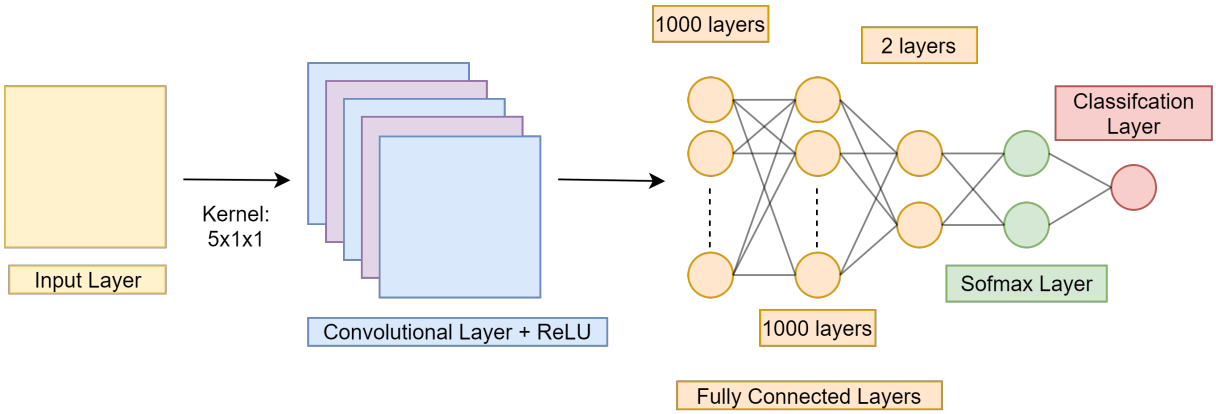

Figure 4.6: CNN classification algorithm used on this dissertation work.

Stochastic Gradient Descent (SGD) is an algorithm that updates the CNN parameters (weights and biases) to minimize the loss function by evaluating the gradient using a subset of the training data. A different subset is used in each iteration. Stochastic gradient descent with momentum (sgdm) described by the equation 4.10 is a SGD algorithm, same as RMSProp (equation 4.11) and adam (equation 4.12) [100, 101].

$$\theta_{l+1} = \theta_l - \alpha \nabla E(\theta_l) + \gamma(\theta_l - \theta_{l-1}) \tag{4.10}$$

$$\theta_{l+1} = \theta_l - \frac{\alpha \nabla E(\theta_l)}{\sqrt{v_l} + \varepsilon} \tag{4.11}$$

$$\theta_{l+1} = \theta_l - \frac{a m_l}{\sqrt{v_l} + \varepsilon} \tag{4.12}$$

4.1.3 Feature Selection

Feature selection or variable selection is an important step in model construction. When building a model, relevant features aren't known a priori. Many features are introduced to better represent the problem domain. However, many of these features are either redundant or irrelevant. It is important to note that these are two distinct notions. A feature can be relevant but redundant because of another relevant feature that is strongly correlated. The use of feature selection techniques comes from the fact original data contains these redundant or irrelevant features and can be removed without the loss of big quantity information. The use of feature selections presents some advantages. It helps with the simplification of models, it can shorten training times and avoid the curse of dimensionality [102].

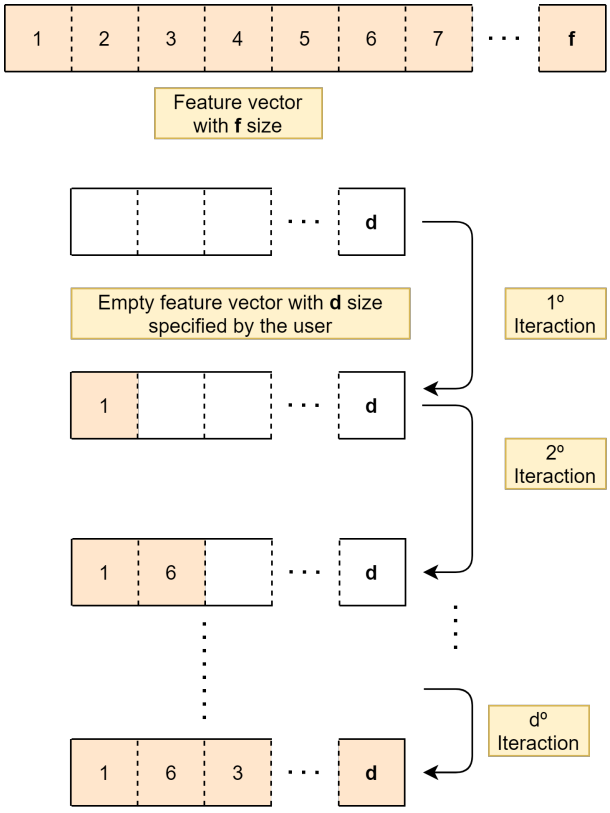

Figure 4.7: Example of a sequential feature selection algorithm.

Feature selection can be supervised, unsupervised or semi-supervised. Supervised feature selection can be subdivided into filter models, wrapper models, and embedded models. Filter models separate the feature selection algorithm from the learning model, to avoid the interaction between the feature selection and learning model bias. The wrapper model uses the predictive properties of the classifier models to determine the quality of the features. This method has a higher computation time. Embedded models were developed to try and bridge the two previous models. It incorporates the

statistical criteria present in the filter method, to select the best features and uses the predictive properties of the wrapper method to select the best subset of features [103].

In the previous paragraph, it was discussed different feature selection methods based on the combination of the feature selection method and machine learning algorithm. The process of selecting the subset of features was never discussed. Kruskal-Wallis one-way analysis of variance is a non-parametric method, being an extension of the Mann-Whitney U test and the parametric equivalent to one-way analysis of variance [104]. Using the p-value as the deciding term, the closest this value is to zero the more discriminative information it contains. This information can be used as a method for a feature selection set. By using the p-value as a threshold, features with a p-value below a certain level are chosen to go into the machine learning algorithm [45].

Sequential feature selection (SFS) is another method to select a subset of features (figure 4.7). Having an empty vector of features, the original features are individually evaluated based on a criterion function with the best one is added to the vector. The remaining features are then individually paired with the selected feature, its performance again evaluated, and the best pair is added. This process is repeated until the vector reaches the desired number of features[105, 106]. Neighborhood component feature selection (NCFS) is a non-parametric method for feature selection. It uses a gradient ascent technique to maximize the expected leave-one-out classification accuracy. It is highly insensitive to a high number of features. The goal of this method is to find a feature subset optimizing the nearest neighbour classification [107].

4.1.4 Cross-Validation

There are various methods to predict how a machine learning model will perform when there isn't independent data. Cross-validation is one of them. It is generally used when there is a need to estimate how accurately a predicted model will perform. This technique is also used to see if there are problems with overfitting or selection bias. Cross-validation involves partitioning the data into subsets, one being the training set used to build the classification model and a second one, the testing set, used to validate the model. In one round cross-validation, this process is only performed once. To reduce the variability, multiples round of cross-validations are performed using cross-validation [108].

Cross-validation has non-exhaustive and exhaustive methods. In non-exhaustive methods, it isn't computed every splitting possibility of the original training set. K-fold cross-validation is a non-exhaustive method. In this method, the original data set is divided into randomly distributed k equal size subsamples. Of the subsamples, one is left as the testing sample, while the others are used as training. Because all examples are used for both training and testing and training exactly once, it is an advantage. Exhaustive cross-validation methods learn as tests all possible ways to divide the originals examples into training and testing subsamples. Leave-one-out cross-validation, an exhaustive method, uses all the examples in a single testing sample. By leaving only one example as

a testing subset, it uses all the other examples as a training subset. The process is repeated n times the number of examples, however, it may require a high computing time [108].

4.1.5 Classification Indexes

A confusion matrix is a table that allows the visualization of the performance of a given algorithm. Different classification index can be calculated based a confusion matrix (Figure 4.8). The accuracy (equation 4.13) of a machine learning algorithm is calculated by averaging the different accuracies obtained using cross validation [108],

$$Accuracy(\%) = \frac{TP+TN}{TP+TN+FP+FN} * 100 \tag{4.13}$$

where TP is the True Positives, TN is the True Negatives, FP is the False Positives, and FN is the False Negatives.

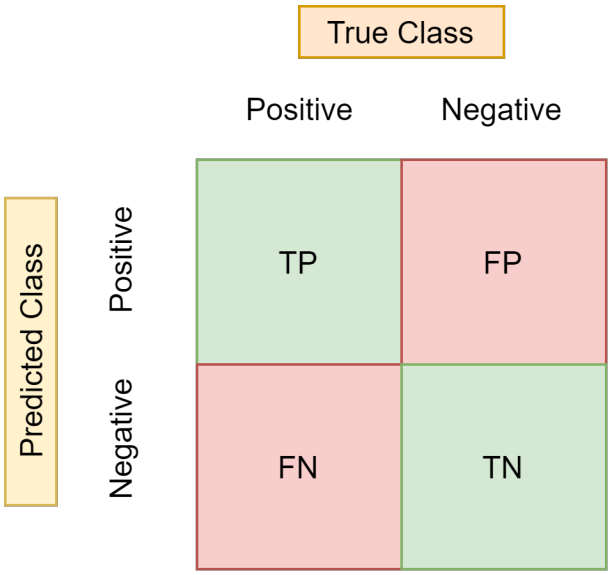

Figure 4.8: Example of a confusion matrix.

CHAPTER 5

Machine and deep learning system for checking wound activity overtime

5.1 Skin Models

FT LARGE Skin Models (Phenion®, Düsseldorf, Germany) were used for the data collection. They were treated in sterile conditions inside a class II biological safety cabinet and were stored in an incubator at 37ºC and 5% carbon dioxide.

Experimental Design

The full experimental design proposed by Phenion® be found in appendix A. The models were grown in individual Petri dishes. A filter spacer was placed inside the Petri dishes, with the pins facing upwards. In each plate, 10 ml of Air-Liquid medium without antibiotics was added, after being pre-heated to a temperature of 37 ºC. A sterile paper filter was placed on top of the spacers allowing the filter to be soaked with the medium.

The skin models were transported on a 6 well plate. The shipping protectors were removed with sterile forceps, grating free access to the full-thickness skin models. Using sterile forceps, the models were transferred to the Petri dishes and placed on top of the paper filters. Extra ALI medium was added in cases where the medium and the filter paper weren't in contact. Each petri dish was covered with a lid and transferred to the incubator. Every two days the medium was changed.

The wounds were made using an 8 mm biopsy dermal punch from *RazorMed™* (Gurgaon, India). To simulate a chronic wound, 200 µL of cultured *S. aureus* was added to the models at a concentration of $9.3 * 10^7$ CFU/mL. However, this process was only simulated in the second round of data collection.

5.2 Sensors

Visual inspection is the primary method to determine the state of a wound. With the development of biosensors, biochemical, chemical, and physical parameters can more easily be monitored. Because the main objective of this thesis is to check the feasibility of using AI and 3D to build a system to discriminate between acute and chronic wound healing, the sensors used were some of the cheapest available options.

Surrounding humidity and temperature were measured using an AM2302 DHT22 sensor, capable of collecting data points with a precision of $\pm 2\%$ and ± 0.5 ºC, respectively. A Flir One Pro LT thermal camera was used to capture thermal images with 80x60 of resolution and, also natural images with a resolution of 1440x1080. The camera has a thermal resolution of 0.1 ºC and thermal sensitivity of 100 mK.

5.3 Data collection method

There were some limitations to the data collection. The skin models could only be out of the incubator for limited periods of time. There was also the risk of contamination due to the contact between the sensors and models, as well as the model with the environment. To avoid environmental contamination the models were handled, this includes changing the medium and data collection, inside a class II microbiology safety cabinet. Before every data collection session, the sensors and Digital Signal Processing unit (DSP) were sterilized using both UV light and 70% alcoholic solution.

To collect the data, the sensors were connected to a breadboard connected to an Arduino UNO® DSP. Each model had a single sensor assigned which would collect the data and an additional sensor would collect the environmental temperature and humidity (Figure 5.1). The DSP is connected to computed stationed outside the cabinet. The thermal photos were taken from a high of 10.3 cm.

Because of these limitations, the models were only out of the incubator for a maximum period of 20 minutes. Right after the model was taken out a thermal image was taken. After this process, the sensors were placed on top of the models and collected the humidity and temperature for 10 minutes at a sampling frequency of 0.3 Hz, resulting in a 1D signal over time. A final thermal image is taken before storing the models inside the incubator. This process was replicated every 2 and half hours, between 8 AM and 6 PM, letting the model rest for the rest of the time.

5.4 The collected Database

The work Database comes from two different data collections. In the first data collection, four models were used with three undergoing the wounding process. The one left out was used as a control. In this data collection *S. aureus* was used to simulate chronic wounds. Instead, using the phenol red present in the ALI medium, if there was a change in the colour of the medium it was a signal that was

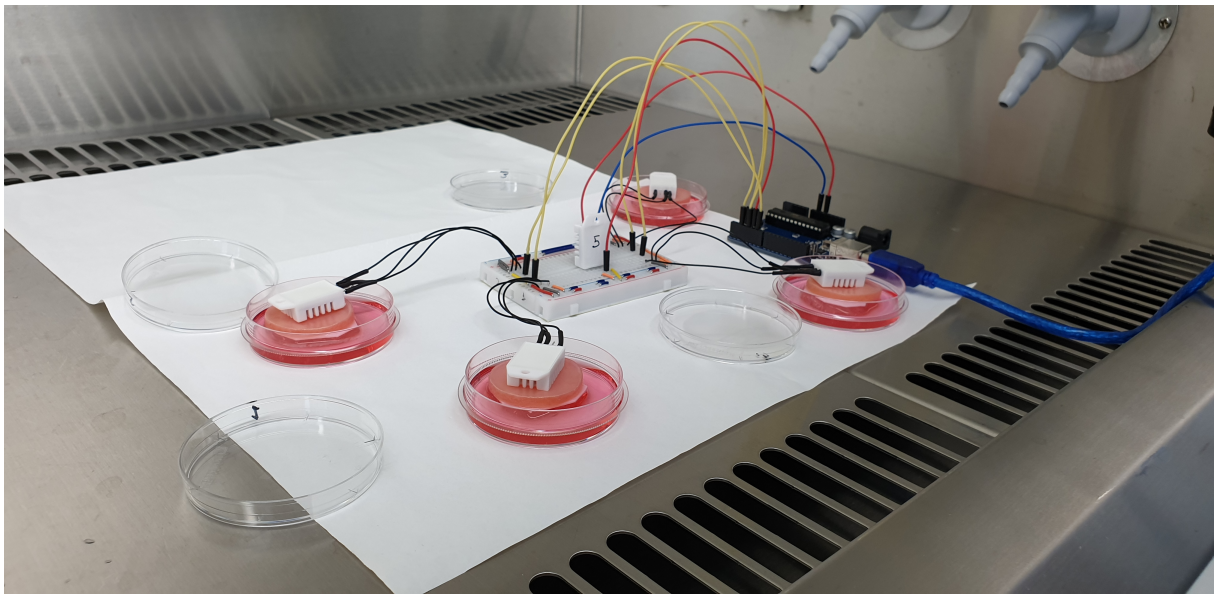

Figure 5.1: Set-up for the humidity and temperature data collection.

infected. Both temperature, humidity, and thermal images were collected during this process. During the second data collection, two models were used. In one of the models, *S. aureus* was added at a concentration of $9.30 * 10^7$ CFU/ml. During this data collection only, thermal images were collected.

Table 5.1: Data Summarization.

Data Collection	Nº of Models	Nº of Humidity Signals	Nº of Temperature Signals	Nº of Thermal Images
1	4	56	56	56
2	2	-	-	66

In table 5.1 the first data collection resulted in 56 signals of humidity and temperature, as well as 56 thermal images. This means that for each model, data were collected at 13 different instances. At the second data by removing the humidity and temperature sensors, it was possible to prolong the life span of the models' thanks to the reduced risk of contamination resulting in 66 thermal images or 33 for each model.

5.5 Methodology

The overall methodology can be found in the figure 5.2. The process started with the construction of a database by data collection and then the data is curated. This process is important since there are two types of signals, 1D (humidity and temperature) and 2D (thermal images). Following the data

curation, pre-processing is applied. After the pre-processing, the signals undergo 1D and 2D signal processing. To the 1D signals, wavelet decomposition is applied, while in the 2D signals different regions of the image are segmented. Features are then extracted to both types of data and organized in matrixes. A feature selection method was applied for screening the best features. The features are then used in supervised machine learning methods and convolutional neural networks to predict wound states. Besides evaluating separately each biosignal, the best features from each signal were integrated as following:

- Humidity and Temperature;
- Humidity and Thermal Images;

where the best features from the humidity sensor and temperature sensor from the different selection method are combined and feed to the different machine learning algorithms. The same process is applied to the humidity and thermal image features. In the following sub-chapters, each step of the process will be discussed in more detail.

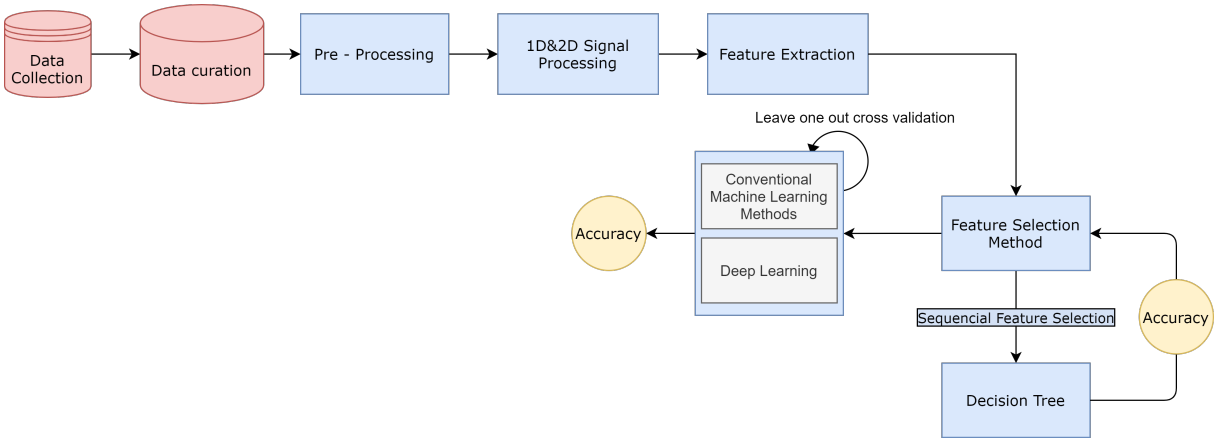

Figure 5.2: Data screening and matrixes organization for classification step.

5.5.1 Pre-Processing

At this point, the data retrieved from the humidity and temperature sensors, as well as thermal cameras was organized. The presence of phenol-red, a pH indicator that exhibits a gradual transition from yellow to pink in a range of 6.8 to 8.2, allows the detection of contamination in the medium from bacteria. The presence of *S. aureus* results in the rapid acidification of the medium, changing the colour from pink to yellow (figure 5.3). This colour change was used to divide the wound states. It was considered a healthy wound healing state when the medium colour was pink (figure 5.3a), and the moment there was a change to yellow it was considered an un-healthy wound healing state (figure 5.3b).

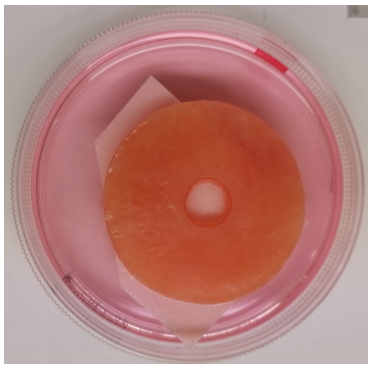

(a) Example of a healthy wound healing state.

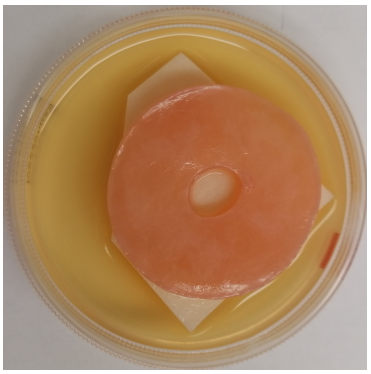

(b) Example of a un-healthy wound healing state.

Figure 5.3: Example of a healthy and un-healthy wound healing states.

A pre-processing is applied to the two types of data. It is important to remember that there are two different types of biosignals humidity and temperature that are affected by the environment. The environmental humidity and temperature were removed from the original signal. A standard score or z-score, a normalization technique, was applied to the humidity signal, based on the equation 5.1,

$$z_i = \frac{x_i - \mu}{\sigma} \tag{5.1}$$

where z_i is the normalized data signal vector, x_i the signal vector, μ signal mean, and σ the standard deviation of x_i. The temperature signal underwent a different pre-processing based on equation 5.2,

$$m_i = x_i - \mu \tag{5.2}$$

where m_i is the resulting temperature signal with the signal mean removed.

The temperatures in the thermal images were converted to a greyscale between [0-255]. By giving the value 0 to the lowest temperature of an image and 255 to the highest temperature, a linear equation is calculated with these two points. The rest of the temperatures are then converted based on the calculated equation.

5.5.2 1D Signal Processing and Feature Extraction

During the signal processing, two different methodologies were idealized specifically tailored to the 1D and 2D signal respectively. Both humidity and temperature signals undergo a three-level discrete wavelet transform (DWT), explained in chapter 5.5.2.1 and represented in figure 5.4, resulting in approximated coefficients (DWT_A^{φ}) and detail coefficients (DWT_D^{Ψ}). Feature are then extracted from each of the reconstructed signals.

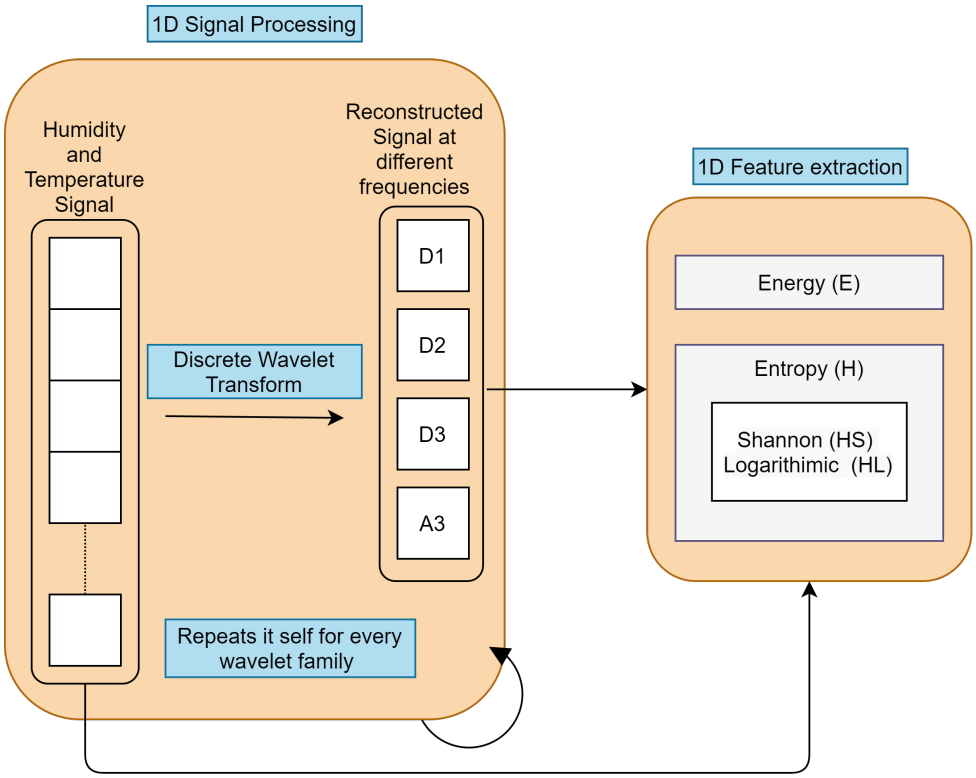

Figure 5.4: 1D Signal Processing and Feature Extraction Diagram.

5.5.2.1 Wavelet Transform and Discrete Wavelet Transform

Wavelet Transform (WT) is used in data analysis when time and frequency resolutions are critical. In low frequencies, it has bad time resolution and good frequency resolution, and inversely at high frequencies, it has good time resolution but bad frequency resolution. The mother WT can be calculated based on equation 5.3,

$$\psi(t)_{(\tau,s)} = \frac{1}{\sqrt{s}} \psi * \left(\frac{t - \tau}{s} \right) \tag{5.3}$$

where $\psi(t)$ is the Wavelet Mother, τ is the transitional parameter and s is the scalar parameter. Small values of s result in the compression of the wavelet allowing to emphasize high-frequency components, while high values of s have the opposite effect on the wavelet, expanding it and allow it emphasize the low-frequency components of the signal [109].

Discrete Wavelet Transform (DWT) consist of obtaining progressively smaller and smaller signal resolutions by successive filtering. A scale function ($\varphi[n]$) and a wavelet function ($\Psi[n]$) are used to

achieve this filtering, as shown in the equation 5.4 and 5.5,

$$\varphi[n] = \sum_k h[n] * \phi[2n-k] \tag{5.4}$$

$$\Psi[n] = \sum_k g[n] * \phi[2n-k] \tag{5.5}$$

where $h[n]$ is the impulse response of the low pass filter and $g[n]$ the impulse response of the high pass filter in WT and k the discrete translation parameter. The decomposition of a signal in different bands is achieved by this successive low-pass and high pass filter followed by downsampling of a factor of 2. The max level of decomposition is given by $\log_2(N)$, where N is the length of a given signal. The reconstructed signals are calculated by the equation 5.6 and 5.7,

$$DWT_A^{\varphi}[j,k] = \sum_{n=0}^{\frac{N}{2^{(j-1)}}} DWT_A^{\varphi}[j-1,n] \bullet h[2k-n] \tag{5.6}$$

$$DWT_D^{\Psi}[j,k] = \sum_{n=0}^{\frac{N}{2^{(j-1)}}} DWT_A^{\varphi}[j-1,n] \bullet g[2k-n] \tag{5.7}$$

where $k = 0,1,...,\frac{N}{2^j}$ and $j = 0,1,...,\log_2 N$. A three-level or scale filter bank can be found in figure 5.5, S represents a discrete signal.

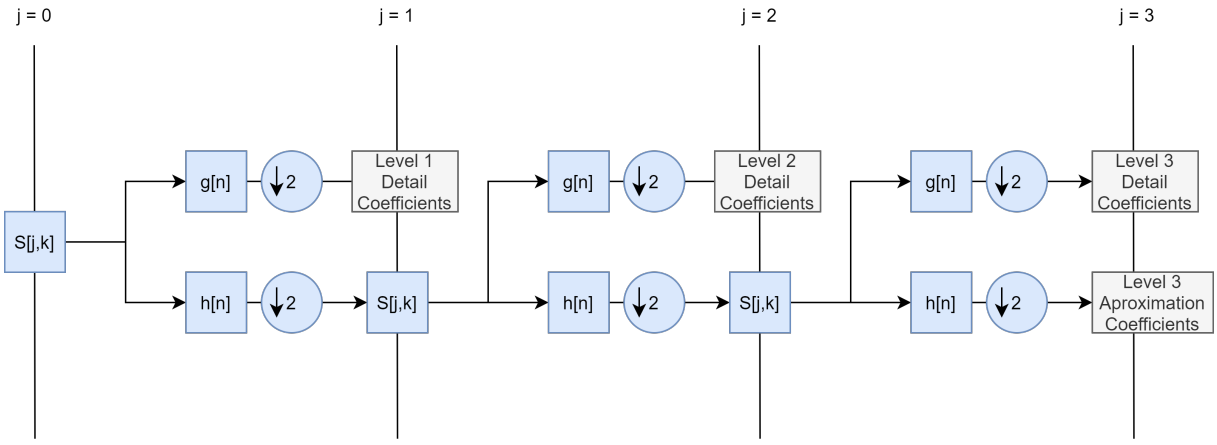

Figure 5.5: A level 3 filter bank.

Different wavelets were proposed throughout the years with the Haar wavelet being described in 1910 by Alfréd Haar [109]. Daubechies, Coiflets, Symlet, Fejér-Korovkin filters, discrete approximation of Meyer Wavelet, biorthogonal and reverse biorthogonal wavelets were used during the development of this work and can be found in appendix B.

5.5.2.2 1D Features

Energy

The signal energy described by the equation 5.8 is a signal pattern feature to evaluate the signal power on a restricted time commonly used to detect the activity of neurological diseases [110].

$$E = \sum_{n=o}^{N} |S[n]|^2 \tag{5.8}$$

Entropy

Entropy measures the "unpredictability" or uncertainty of a given system and measures its level of chaos. High levels of entropy indicate a more complex or chaotic system thus being less predictable. Shannon Entropy (equation 5.9) and logarithmic entropy (equation 5.10) are some of the entropies that are possible to compute from a given signal [111].

$$HS = -\sum_{n=o}^{N} |S[n]|^2 * \log_{10}\left(|S[n]|^2\right) \tag{5.9}$$

$$HL = \sum_{n=o}^{N} \log_{10}\left(|S[n]|^2\right) \tag{5.10}$$

5.5.3 2D Signal Processing and Feature Extraction

The methodology idealized for the 2D signals was simpler when compared to 1D signals. Three circular regions of interest were identified in the greyscale images of the thermal images. The overall skin model, this is, both the skin tissue area and the wound region area, only the skin tissue region and only the wound region, as represented in figure 5.6. The skin tissue region can be considered the surrounding tissue of a wound.

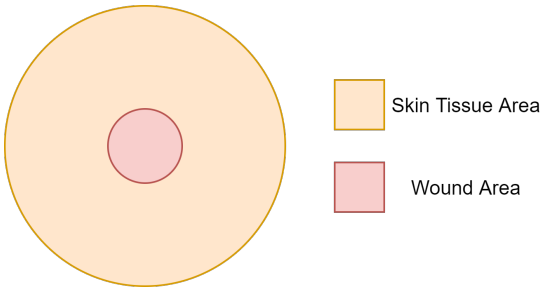

Figure 5.6: Skin model areas of interest representation.

These regions were manually extracted by selecting four points in the thermal image, two horizontally ($z1$ and $z2$) and two vertically ($z3$ and $z4$). Two straight lines ($l1$ and $l2$) are then calculated using the two pair of points, with the intersection between the lines being defined as the

center of a region of interest ($C1$) (figure 5.7). The Euclidean distance of both pair of points is then calculated, with its means used as the region of interest. These computations were possible for both the skin model and wound regions, the skin tissue region was calculated by subtracting the wound region to the skin model region. However, all these calculations were done on the converted greyscale image. These images are then converted to 3 binary images and then each element has been multiplied point by point with the respective ones from the original thermal images. With this process, the temperature of each defined region has been retrieved.

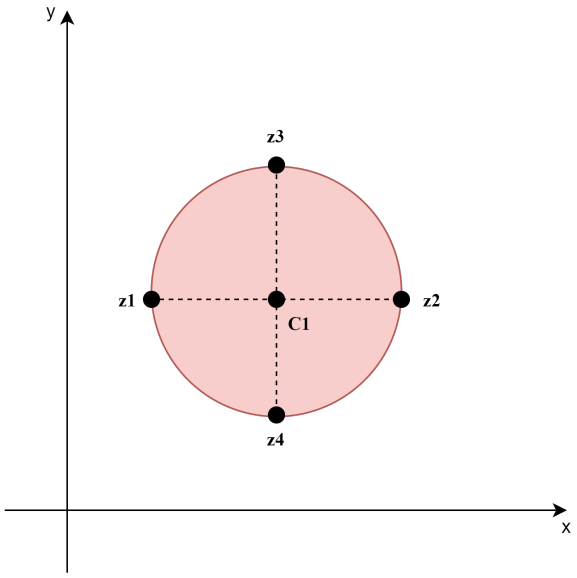

Figure 5.7: Example of a point selection and calculation of the center of the wound region.

Statistical features such as arithmetic mean (equation 5.11), median (equation 5.12), variance (equation 5.13), standard deviation (equation 5.14), skewness (equation 5.15), kurtosis (equation 5.16) and percentile at 5 % and 95 % (equation 5.17) are then extracted from each region,

$$\bar{x} = \frac{\sum_{i=1}^{r}\sum_{j=1}^{c} I(i,j)}{m} \tag{5.11}$$

$$M = \begin{cases} I\left[\frac{m}{2}\right] + I\left[\frac{m+1}{2}\right], \ if \ m \ is \ even \\ I\left[\frac{m+1}{2}\right], \ if \ m \ is \ odd \end{cases} \tag{5.12}$$

$$V^2 = \frac{\sum_{i=1}^{r}\sum_{j=1}^{c} (I(i,j) - \mu)^2}{m} \tag{5.13}$$

$$\sigma = \sqrt{\frac{\sum_{i=1}^{r}\sum_{j=1}^{c} (I(i,j) - \mu)^2}{m}} \tag{5.14}$$

$$Sk = \frac{\frac{1}{m}\sum_{i=1}^{r}\sum_{i=j}^{r}(I(i,j)-\mu)^3}{(\sqrt{\frac{1}{m}\sum_{i=1}^{r}\sum_{i=j}^{r}(I(i,j)-\mu)^2})^2} \tag{5.15}$$

$$K = \frac{\frac{1}{m}\sum_{i=1}^{r}\sum_{i=j}^{r}(I(i,j)-\mu)^4}{(\sqrt{\frac{1}{m}\sum_{i=1}^{r}\sum_{i=j}^{r}(I(i,j)-\mu)^2})^2} \tag{5.16}$$

$$P(p) = \frac{d}{100} * m \tag{5.17}$$

where c and r representing the position of a given pixel in a thermal image of the region of interest I. The term m represents the total number of pixels for each region of interest, while p corresponds to the desired percentage in the percentile.

Three more feature collections were done in the thermal pictures, where different processes were applied to the original pixel values. A logarithm of 2, 10, and a natural logarithm are applied to values of the pixel with the same features being calculated after which process (Figure 5.8).

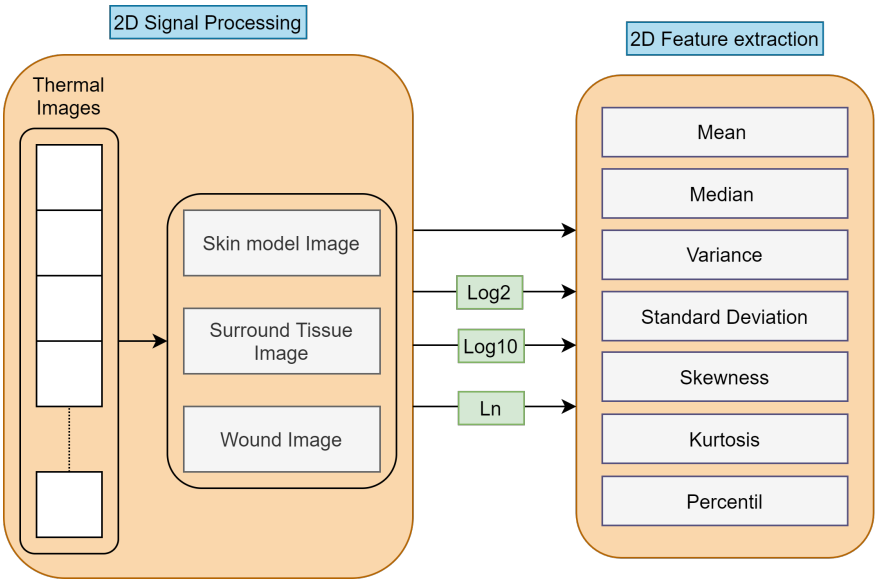

Figure 5.8: 2D Signal Processing and Feature Extraction Diagram..

5.5.4 1D & 2D Feature Selection and predictive models

From the feature extraction methodology, 192 features were extracted from thermal images and 1102 from humidity and temperature signals respectively. Because of the high number of features extracted, a feature selection methodology was developed, one specific for humidity/temperature signals and another one for thermal images.

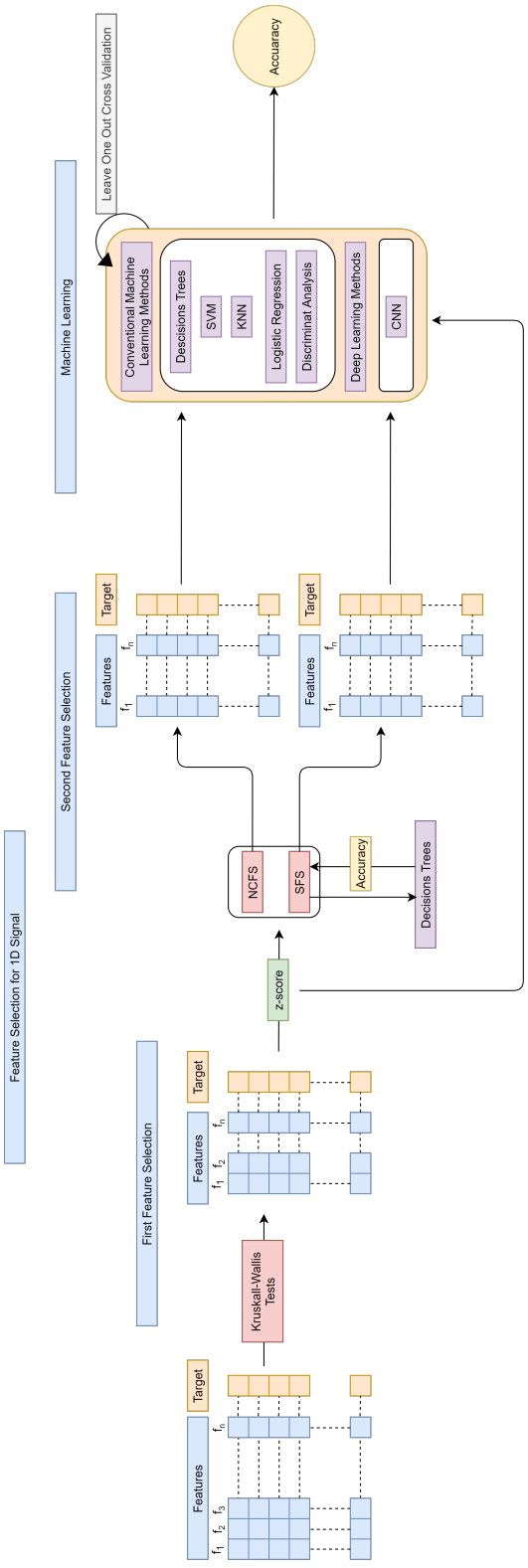

Figure 5.9: Feature selection and machine learning algorithm methodology for 1D signals.

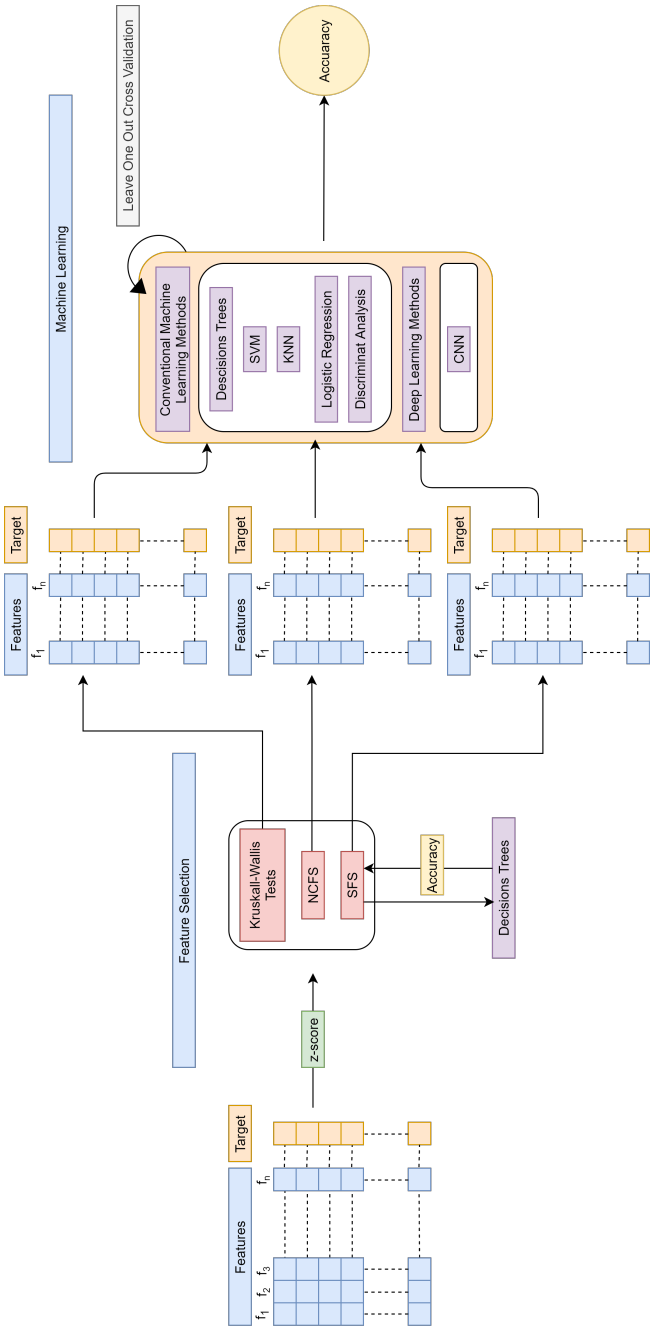

Figure 5.10: Feature selection and machine learning algorithm methodology for 2D signals.

The resulting features extracted from the temperature and humidity signals are then subject to the feature selection method as shown in figure 5.9. But before it, the Kruskal-Wallis test was applied, in order to reduce the number of features. Just those that presented significant distributions ($p<0.05$) to distinguish normal wounds and chronic wounds have been selected for the next phase. A z-score is then applied to the resulting features. In appendix C the same methodology can be found without the z-score normalization step (Figure C.1 and figure C.2). By normalizing the features it is expected the performance of the machine learning algorithms to improve by standardizing the different features that describe wound models. The features resulting from the Kruskal-Wallis test undergo a second feature selection process, where the best features are selected based on an NCFS and SFS method.

From the SFS it results in 200 sequentially ranked features based on the performance at differentiating wounds states. Features derived from the SFS method were provided to the decision tree machine learning algorithm with leave one out cross-validation and its performance was evaluated. Accuracy resulting from decision trees was used to select the best length sequence of features. Decision trees can be some of the simplest machine learning methods and as result accuracies can be lower, still it was used due to its fast computation time. This may result in a better performance from the decision tree algorithms when compared to other methods. Using the NCFS method a value is attributed to the performance of the features at differentiating the wounds. Most features had a performance close to 10^{-10}, so features with performance better than 0.01 were selected.

Table 5.2: Traditional Machine Learning Algorithms and its parameters.

Machine Learning Algorithm Family	Denomination of the algorithm	Explanation of the parameters used.
Decisions Trees	Fine Tree	There are maximum of 100 nodes.
	Medium Tree	There are maximum of 20 nodes.
	Coarse Tree	There are a maximum of 4 nodes.
SVM	Linear SVM	Uses a linear kernel type.
	Quadratic SVM	Uses a polynomial kernel typed of 2^{nd} order.
	Cubic SVM	Uses a polynomial kernel typed of 3^{rd} order.
	Fine Gaussian SVM	Uses a Gaussian kernel with a scale function equal to the square root of the number of features divided by 4.
	Medium Gaussian SVM	Uses a Gaussian kernel with a scale function equal to the square root of the number of features.
	Coarse Gaussian SVM	Uses a Gaussian kernel with a scale function equal to the square root of the number of features multiplied by 4.
KNN	Fine KNN	Uses the euclidean distance calculate the distance between to samples with k neighbours equal to 1.
	Medium KNN	Uses the euclidean distance calculate the distance between to samples with k neighbours equal to 10.
	Cosine KNN	Uses the cosine distance to calculate the distance between to samples with k neighbours equal to 10.
	Cubic KNN	Uses the cubic distance to calculate the distance between to samples with k neighbours equal to 10.
	Weighted KNN	Uses the weighted distance to calculate the distance between to samples with k neighbours equal to 10.

Since only 192 features were extracted from the thermal images, the Kruskal-Wallis test was used to find the best selection of features that best differentiate between an acute and chronic wound ($p<0.05$). The threshold for the NCFS method was 0.01, and it used the accuracies from decision tree algorithms to find the best length of features in the SFS method. Also, an option of using all the

features to train the machine learning algorithm was included. The option of applying a z-score to the original features before the feature selection was present. Figure 5.10 shows the feature selection method and machine learning algorithm methodology for 2D signals.

Different machine learning algorithms were used to predict a wound state. Inside each family of machine learning algorithms, different parameters were used. Table 5.2 summarizes these parameters. Due to the low number of samples, the machine learning algorithms are built-in leave-one-out cross-validation to improve the robustness of the algorithms built.

5.5.5 Accuracies of the predictive models

Different machine learning algorithms were used to predict wound healing states, and the best accuracies for each sensor can be found in appendix D.

Table 5.3 summarizes the best performing machine learning algorithms at differentiating between a healthy and not healthy wound healing state using only humidity and temperature features, as well as, a combination of both, and a combination of humidity and thermal image features, with the full results for the traditional machine learning algorithms found in table D.1, table D.2, table D.3 and table D.4. From the analysis of the table 5.3 some conclusions can be drawn: (1) KNN algorithms fed with features extracted from humidity time-series reached an accuracy of 75% without z-score step and 71.4% with z-score step. (2) The combination of temperature signal features provided a maximum accuracy of 83.9% when applied without z-score step to the KKN entries and 83.9% when normalized with z-score and applied to Coarse Gaussian SVM or a weighted KNN.

Table 5.3: Traditional machine learning algorithms according to its performances.

Biosensor	**z-score Application**	**Feature Selection**	**Machine Learning Algorithm**	**Accuracy (%)**
Humidity	No	SFS	Cubic KNN	71.4
	Yes	NCFS	Cubic KNN	75.0
Temperature	No	SFS	Cosine KNN	83.9
	Yes	NCFS	Coarse Gaussian SVM/ Weighted KNN	83.9
Humidity + Temperature	No	SFS/ SFS	Cosine KNN	83.9
	Yes	NCFS/ NCFS	LR	85.7
Humidity + Thermal Images	No	NCFS/ SFS	Linear SVM	83.3
	Yes	NCFS/ SFS	LD / Linear SVM	81.3

One change that the application of z-score brought was in the feature selection method used before the machine learning algorithm. SFS was the feature selection method of choice for machine

learning algorithms without the z-score step while traditional machine learning algorithms performed better with NCFS, instead of SFS. KNN algorithms operate better with features from a single sensor, with a specific SVM, the Coarse Gaussian SVM, being able to match its accuracy.

With the best humidity and thermal features together, the machine learning algorithms reached 81.3% and 83.3% accuracy with and without the application of the normalization step. However, with the mixing of temperature and humidity features, there was a small increase in the best-performing machine learning algorithm, reaching 85.7% with the z-score step and 83.9% without it. The application of the z-score to the features still influences the feature selection method where the application of the step favours the NCFS, while the omission of it favours the SFS. Something to note is that this step didn't have the same effect on the best feature selection method as the previous methods. Instead of the application of the step favour the NCFS method, there wasn't an effect on the normalization on the feature selection method, with the humidity features performing better with NCFS method and thermal images with the SFS method. SVM machine learning algorithms performed better with mixed features, while KNN performed better with singular features. Still, the highest achieving accuracy of 85.7% used a LR algorithm.

The performance of the deep learning algorithms (Table 5.4 and table D.5) was on average worst when compared to the traditional machine learning algorithms. The adam SGD algorithm only obtained a 76.8% using temperature features selected by the SFS method without a z-score normalization while the SGD algorithm RMSProp reached 78.6% using features computed from the temperature features. While on average the deep learning algorithms didn't perform as strongly as the traditional ones, achieved the same accuracy, reaching 85.7% using a combination of humidity and temperature features. One similarity with traditional machine learning is that NCFS performed better at selecting the best features humidity and temperature features to differentiate between a healthy and unhealthy wound state.

Table 5.4: CNN algorithms according to its performances.

Biosensor	z-score Application	Feature Selection	SGD Algorithm	Accuracy (%)
Humidity	No	NCFS	adam	59.0
	Yes	NCFS	sgdm	75.0
Temperature	No	SFS	adam	76.8
	Yes	NCFS / SFS	sgdm / RMSprop	78.6
Humidity + Temperature	No	SFS / SFS	RMSprop	76.8
	Yes	NCFS / NCFS	sgdm	85.7
Humidity + Thermal Images	No	SFS / NCFS	sgdm	72.9
	Yes	SFS / SFS	sgdm / RMSprop	72.9

A thermal camera was another sensor used to try and predict a wound state. Obtaining 2D images allow a thermal mapping of the wound area, something that wasn't possible only using a temperature sensor. Still, while the results obtained using thermal image features (Table 5.5, table D.6, D.7). With

a maximum of 73.2% accuracy using the thermal features from the first data collections. However, there was an improvement in accuracy from the first data collection to the second reaching 80.3%, giving some validation to the approach used during this work for wound healing state prediction and tracking. This performance improvement was noticed in the traditional machine learning algorithms, with decision trees, LD, and LR showing that they are options for wound healing state prediction using thermal images, as well as, in CNN algorithms where their accuracies when from 67.9% to 72.7%. Another interesting aspect was the fact that not using a feature selection method to differentiate the best features performed better in some cases, however, this has some implications. Extracting and combining all features without a features selection step makes the process more complex and the algorithm will take more time to deliver the result when compared with an algorithm optimized with a feature selection tool.

Table 5.5: Comparison between the 1^{st} and 2^{nd} data collection with the thermal image sensor

Data collection	z-score Application	Feature Selection	Machine Learning Algorithm	Accuracy (%)
Traditional Machine Learning Algorithms				
1st	No	NCFS	LR	73.2
	Yes	NCFS / Kruskal Wallis	LD / LR	71.4
2nd	No	No feature selection used	Cubic KNN	77.3
	Yes	SFS	Fine Trees/ Medium Tree	80.3
Convolutional Neural Networks Algorithms				
1st	No	Kruskal - Wallis	sgdm	66.1
	Yes	SFS	sgdm / adam	67.9
2nd	No	SFS	RMSprop	72.7
	Yes	No feature selection used	adam / RMSprop	71.2

While it isn't possible to do a direct comparison between the results of state of art and the ones achieved, figure 5.11 shows the accuracy achieved in other works compared to the one developed. This different approach where another group of sensors is used to try to differentiate different wound healing states surpassed some of the developed work, by reaching 85.7% accuracy.

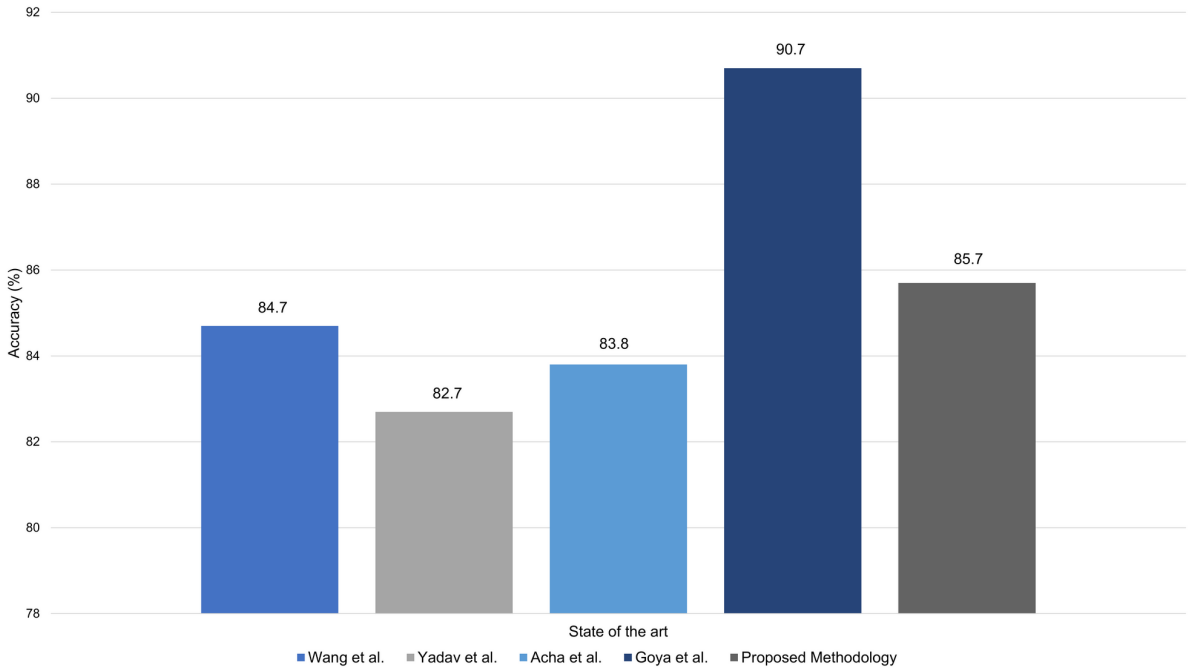

Figure 5.11: Example of Linear SVM classification.

CHAPTER 6

Conclusion

Chronic wounds are a problem that affects millions of people around the world, that results in loss of function and decreased quality of life. In this kind of pathologies the timelier the treatment, the better the outcome to a patient. The development of an application that allows the gathering of information of biomarkers from a wound and predicts its state is a powerful tool since allows for timelier interventions. The features collected from different sensors are used to construct a machine learning algorithm capable of predicting wound states. The work done showed that this approach has potential. Reaching 85.7% accuracy in predicting a wound state, similar to other methodologies showed the viability of this methodology.

However, the results obtained do need to be contextualized. Firstly the low number of 3D skin models used; while it reached 85.7% accuracy using a combination of features from the humidity and temperature sensors, due to the low number of 3D skin models used, it isn't possible to make assumptions on how it would behave in a real patient. Secondly, since 3D models were used, only a small part of the skin was represented. Blood vessels, hair follicles, and sebaceous glands aren't present in the models, as well as, neutrophils and monocytes cells, important defense mechanisms of the skin, all important factors in wound development. Still, the present work presents a proof of concept, and 85.7% accuracy can be considered a success and showcases the potential of using biosensors in combination with machine learning algorithms to predict wound states.

Future works

Chronic wounds are a pathology that affects millions of people, so the development of a diagnostic tool to improve the success of wound treatment is need. Future work is needed to improve the robustness of the methodology proposed. On the following points some tasks are left to be considered as future work research lines:

- Using 3D skin models reduced several problems that would arise while trying to collect data

from a real patient but have the drawback of not considering other factors that affect wound healing. Data collection in real patients is needed to improve and validate this approach.

- Construction of a larger database with different pathologies such as venous ulcer, diabetic foot ulcer, burns, infections and others.
- Using other biosensors that collect different biomarkers from wounds.
- Finding the best combination of sensors that allow a better prediction of a wound state.
- Focusing on one type of machine learning algorithm and optimizing it.

Bibliography

[1] C. K. Sen, G. M. Gordillo, S. Roy, R. Kirsner, L. Lambert, T. K. Hunt, F. Gottrup, G. C. Gurtner, and M. T. Longaker. "Human skin wounds: a major and snowballing threat to public health and the economy". In: *Wound repair and regeneration* 17.6 (2009), pp. 763–771.

[2] C. Lindholm and R. Searle. "Wound management for the 21st century: combining effectiveness and efficiency". In: *International wound journal* 13 (2016), pp. 5–15.

[3] E Pina, K Furtado, P. Franks, and C. Moffatt. "Leg ulceration in Portugal: prevalence and clinical history". In: *European journal of vascular and endovascular surgery* 29.5 (2005), pp. 549–553.

[4] M Augustin and K Maier. "Psychosomatic aspects of chronic wounds". In: *Dermatology and Psychosomatics/Dermatologie und Psychosomatik* 4.1 (2003), pp. 5–13.

[5] S. L. Percival, C. Emanuel, K. F. Cutting, and D. W. Williams. "Microbiology of the skin and the role of biofilms in infection". In: *International wound journal* 9.1 (2012), pp. 14–32.

[6] A. L. Byrd, Y. Belkaid, and J. A. Segre. "The human skin microbiome". In: *Nature Reviews Microbiology* 16.3 (2018), p. 143.

[7] C. Griffiths, J. Barker, T. O. Bleiker, R. Chalmers, and D. Creamer. *Rook's textbook of dermatology*. John Wiley & Sons, 2016.

[8] J. Kanitakis. "Anatomy, histology and immunohistochemistry of normal human skin". In: *European journal of dermatology* 12.4 (2002), pp. 390–401.

[9] M. J. Randall, A. Jüngel, M. Rimann, and K. Wuertz-Kozak. "Advances in the Biofabrication of 3D Skin in vitro: Healthy and Pathological Models". In: *Frontiers in bioengineering and biotechnology* 6 (2018), p. 154.

[10] S. Baranoski. "Skin tears: the enemy of frail skin". In: *Advances in skin & wound care* 13.3 (2000), p. 123.

[11] J. A. Segre et al. "Epidermal barrier formation and recovery in skin disorders". In: *The Journal of clinical investigation* 116.5 (2006), pp. 1150–1158.

[12] Z. Nemes and P. M. Steinert. "Bricks and mortar of the epidermal barrier". In: *Experimental & molecular medicine* 31.1 (1999), pp. 5–19.

[13] C. Blanpain and E. Fuchs. "Epidermal stem cells of the skin". In: *Annu. Rev. Cell Dev. Biol.* 22 (2006), pp. 339–373.

[14] L. M. Biga, S. Dawson, A. Harwell, R. Hopkins, J. Kaufmann, M. LeMaster, P. Matern, K. Morrison-Graham, D. Quick, and J. Runyeon. "Anatomy & physiology". In: (2020).

[15] A. Baroni, E. Buommino, V. De Gregorio, E. Ruocco, V. Ruocco, and R. Wolf. "Structure and function of the epidermis related to barrier properties". In: *Clinics in dermatology* 30.3 (2012), pp. 257–262.

[16] E. Proksch, J. M. Brandner, and J.-M. Jensen. "The skin: an indispensable barrier". In: *Experimental dermatology* 17.12 (2008), pp. 1063–1072.

[17] G. E. Pierard, V. Goffin, T. Hermanns-Le, and C. Pierard-Franchimont. "Corneocyte desquamation." In: *International journal of molecular medicine* 6.2 (2000), pp. 217–238.

[18] T. Egelrud. "Desquamation in the stratum corneum." In: *Acta Dermato-Venereologica* 80 (2000).

[19] E. A. Grice and J. A. Segre. "The skin microbiome". In: *Nature reviews microbiology* 9.4 (2011), pp. 244–253.

[20] R. R. Roth and W. D. James. "Microbiology of the skin: resident flora, ecology, infection". In: *Journal of the American Academy of Dermatology* 20.3 (1989), pp. 367–390.

[21] M. D. Grogan, C. Bartow-McKenney, L. Flowers, S. A. Knight, A. Uberoi, and E. A. Grice. "Research techniques made simple: profiling the skin microbiota". In: *Journal of Investigative Dermatology* 139.4 (2019), pp. 747–752.

[22] C. Gong, Q. Wu, Y. Wang, D. Zhang, F. Luo, X. Zhao, Y. Wei, and Z. Qian. "A biodegradable hydrogel system containing curcumin encapsulated in micelles for cutaneous wound healing". In: *Biomaterials* 34.27 (2013), pp. 6377–6387.

[23] P. Chandika, S.-C. Ko, and W.-K. Jung. "Marine-derived biological macromolecule-based biomaterials for wound healing and skin tissue regeneration". In: *International journal of biological macromolecules* 77 (2015), pp. 24–35.

[24] S. a. Guo and L. A. DiPietro. "Factors affecting wound healing". In: *Journal of dental research* 89.3 (2010), pp. 219–229.

[25] S. Enoch and D. J. Leaper. "Basic science of wound healing". In: *Surgery (Oxford)* 26.2 (2008), pp. 31–37.

[26] M. B. Witte and A. Barbul. "General principles of wound healing". In: *Surgical Clinics of North America* 77.3 (1997), pp. 509–528.

[27] L. Braiman-Wiksman, I. Solomonik, R. Spira, and T. Tennenbaum. "Novel insights into wound healing sequence of events". In: *Toxicologic pathology* 35.6 (2007), pp. 767–779.

[28] B. Busse. "Introduction to wound healing". In: *Wound Management in Urgent Care*. Springer, 2016, pp. 1–5.

[29] C. J. Doillon, M. G. Dunn, E. Bender, and F. H. Silver. "Collagen fiber formation in repair tissue: development of strength and toughness". In: *Collagen and related research* 5.6 (1985), pp. 481–492.

[30] K. Kirketerp-Møller, K. Zulkowski, and G. James. "Chronic wound colonization, infection, and biofilms". In: *Biofilm infections*. Springer, 2011, pp. 11–24.

[31] S Schreml, R. Szeimies, S Karrer, J Heinlin, M Landthaler, and P Babilas. "The impact of the pH value on skin integrity and cutaneous wound healing". In: *Journal of the European Academy of Dermatology and Venereology* 24.4 (2010), pp. 373–378. ISSN: 0926-9959.

[32] R. S. Kirsner and W. H. Eaglstein. "The wound healing process". In: *Dermatologic clinics* 11.4 (1993), pp. 629–640. ISSN: 0733-8635.

[33] B. C. Nwomeh, D. R. Yager, and I. K. Cohen. "Physiology of the chronic wound". In: *Clinics in plastic surgery* 25.3 (1998), pp. 341–356. ISSN: 0094-1298.

[34] J. E. Grey, K. G. Harding, and S. Enoch. "Pressure ulcers". In: *Bmj* 332.7539 (2006), pp. 472–475. ISSN: 0959-8138.

[35] R. E. Pecoraro, G. E. Reiber, and E. M. Burgess. "Pathways to diabetic limb amputation: basis for prevention". In: *Diabetes care* 13.5 (1990), pp. 513–521. ISSN: 0149-5992.

[36] W. Clayton and T. A. Elasy. "A review of the pathophysiology, classification, and treatment of foot ulcers in diabetic patients". In: *Clinical diabetes* 27.2 (2009), pp. 52–58. ISSN: 0891-8929.

[37] C. K. Bowering. "Diabetic foot ulcers. Pathophysiology, assessment, and therapy." In: *Canadian Family Physician* 47.5 (2001), pp. 1007–1016. ISSN: 0008-350X.

[38] L. S. Weyrich, S. Dixit, A. G. Farrer, A. J. Cooper, and A. J. Cooper. "The skin microbiome: associations between altered microbial communities and disease". In: *Australasian journal of dermatology* 56.4 (2015), pp. 268–274. ISSN: 0004-8380.

[39] M. N. Storm-Versloot, C. G. Vos, D. T. Ubbink, and H. Vermeulen. "Topical silver for preventing wound infection". In: *Cochrane Database of Systematic Reviews* 3 (2010). ISSN: 1465-1858.

[40] R. Serra, R. Grande, L. Butrico, A. Rossi, U. F. Settimio, B. Caroleo, B. Amato, L. Gallelli, and S. de Franciscis. "Chronic wound infections: the role of Pseudomonas aeruginosa and Staphylococcus aureus". In: *Expert review of anti-infective therapy* 13.5 (2015), pp. 605–613. ISSN: 1744-8336.

[41] A. R. Siddiqui and J. M. Bernstein. "Chronic wound infection: facts and controversies". In: *Clinics in dermatology* 28.5 (2010), pp. 519–526. ISSN: 0738-081X.

[42] E. Heuss. *Die reaktion des schweisses beim gesunden menschen*. Voss, 1892.

[43] M. O. Visscher, R. Chatterjee, K. A. Munson, W. L. Pickens, and S. B. Hoath. "Changes in diapered and nondiapered infant skin over the first month of life". In: *Pediatric dermatology* 17.1 (2000), pp. 45–51. ISSN: 0736-8046.

[44] G. Yosipovitch, A. Maayan-Metzger, P. Merlob, and L. Sirota. "Skin barrier properties in different body areas in neonates". In: *Pediatrics* 106.1 (2000), pp. 105–108. ISSN: 0031-4005.

[45] S. M. Ali and G. Yosipovitch. "Skin pH: from basic science to basic skin care". In: *Acta dermato-venereologica* 93.3 (2013), pp. 261–269. ISSN: 0001-5555.

[46] B. Dréno, S. Pécastaings, S. Corvec, S. Veraldi, A. Khammari, and C. Roques. "Cutibacterium acnes (Propionibacterium acnes) and acne vulgaris: a brief look at the latest updates". In: *Journal of the European Academy of Dermatology and Venereology* 32 (2018), pp. 5–14. ISSN: 0926-9959.

[47] H. C. Korting, O Braun-Falco, E Ponce-Pöschl, W Klövekorn, G Schmötzer, and M Arens-Corell. "The influence of the regular use of a soap or an acidic syndet bar on pre-acne". In: *Infection* 23.2 (1995), pp. 89–93. ISSN: 0300-8126.

[48] S. L. Percival, S. McCarty, J. A. Hunt, and E. J. Woods. "The effects of pH on wound healing, biofilms, and antimicrobial efficacy". In: *Wound Repair and Regeneration* 22.2 (2014), pp. 174–186. ISSN: 1067-1927.

[49] G Roberts. "Physical changes in dermal tissues around leg ulcers". In: *Proceedings of the 7th European Conference on Wound Management*. 1997, pp. 104–105.

[50] R Hoffman, J Noble, and M Eagle. "The use of proteases as prognostic markers for the healing of venous leg ulcers". In: *Journal of wound care* 8.6 (1999), pp. 273–276.

[51] V. K. Shukla, D Shukla, S. K. Tiwary, S Agrawal, and A Rastogi. "Evaluation of pH measurement as a method of wound assessment". In: *Journal of wound care* 16.7 (2007), pp. 291–294. ISSN: 0969-0700.

[52] M. Fierheller and R. G. Sibbald. "A clinical investigation into the relationship between increased periwound skin temperature and local wound infection in patients with chronic leg ulcers". In: *Advances in skin & wound care* 23.8 (2010), pp. 369–379. ISSN: 1527-7941.

[53] C. R. Kruse, K. Nuutila, C. C. Y. Lee, E. Kiwanuka, M. Singh, E. J. Caterson, E. Eriksson, and J. A. Sørensen. "The external microenvironment of healing skin wounds". In: *Wound Repair and Regeneration* 23.4 (2015), pp. 456–464. ISSN: 1067-1927.

[54] M. Denda, T. Sokabe, T. Fukumi-Tominaga, and M. Tominaga. "Effects of skin surface temperature on epidermal permeability barrier homeostasis". In: *Journal of Investigative Dermatology* 127.3 (2007), pp. 654–659. ISSN: 0022-202X.

[55] K. A. Engebretsen, J. D. Johansen, S Kezic, A Linneberg, and J. P. Thyssen. "The effect of environmental humidity and temperature on skin barrier function and dermatitis". In: *Journal of the European Academy of Dermatology and Venereology* 30.2 (2016), pp. 223–249. ISSN: 0926-9959.

[56] F. Hackl, J. Bergmann, S. R. Granter, T. Koyama, E. Kiwanuka, B. Zuhaili, B. Pomahac, E. J. Caterson, J. P. E. Junker, and E. Eriksson. "Epidermal regeneration by micrograft transplantation with immediate 100-fold expansion". In: *Plastic and Reconstructive Surgery* 129.3 (2012), 443e–452e. ISSN: 0032-1052.

[57] H. Niehues, J. A. Bouwstra, A. El Ghalbzouri, J. M. Brandner, P. L. J. M. Zeeuwen, and E. H. van den Bogaard. "3D skin models for 3R research: The potential of 3D reconstructed skin models to study skin barrier function". In: *Experimental dermatology* 27.5 (2018), pp. 501–511. ISSN: 0906-6705.

[58] J. G. Rheinwatd and H. Green. "Seria cultivation of strains of human epidemal keratinocytes: the formation keratinizin colonies from single cell is". In: *Cell* 6.3 (1975), pp. 331–343. ISSN: 0092-8674.

[59] D. Antoni, H. Burckel, E. Josset, and G. Noel. "Three-dimensional cell culture: a breakthrough in vivo". In: *International journal of molecular sciences* 16.3 (2015), pp. 5517–5527.

[60] B. De Wever, D. Petersohn, and K. R. Mewes. "Overview of human three-dimensional (3D) skin models used for dermal toxicity assessment (Part 1)". In: *Household and Personal Care Today* 8.1 (2013), pp. 18–22.

[61] P. Salvo, V. Dini, F. Di Francesco, and M. Romanelli. "The role of biomedical sensors in wound healing". In: *Wound Medicine* 8 (2015), pp. 15–18. ISSN: 2213-9095.

[62] S. Koerner, D. Adams, S. L. Harper, J. M. Black, and D. K. Langemo. "Use of thermal imaging to identify deep-tissue pressure injury on admission reduces clinical and financial burdens of hospital-acquired pressure injuries". In: *Advances in skin & wound care* 32.7 (2019), p. 312.

[63] R. Priemer. *Introductory signal processing*. Vol. 6. World Scientific, 1991. ISBN: 9971509199.

[64] F. J. Theis and A. Meyer-Bäse. *Biomedical signal analysis: Contemporary methods and applications*. MIT Press, 2010. ISBN: 0262013282.

[65] J. L. Semmlow and B. Griffel. *Biosignal and medical image processing*. CRC press, 2014. ISBN: 1466567376.

[66] C Magalhaes, R. Vardasca, and J Mendes. "Recent use of medical infrared thermography in skin neoplasms". In: *Skin Research and Technology* 24.4 (2018), pp. 587–591. ISSN: 0909-752X.

[67] M. Planck. *The theory of heat radiation*. Courier Corporation, 2013. ISBN: 0486173283.

[68] J. T. Costello, C. D. McInerney, C. M. Bleakley, J. Selfe, and A. E. Donnelly. "The use of thermal imaging in assessing skin temperature following cryotherapy: a review". In: *Journal of Thermal Biology* 37.2 (2012), pp. 103–110. ISSN: 0306-4565.

[69] J. J. van Netten, J. G. van Baal, C. Liu, F. van Der Heijden, and S. A. Bus. *Infrared thermal imaging for automated detection of diabetic foot complications*. 2013.

[70] T. R. Dargaville, B. L. Farrugia, J. A. Broadbent, S. Pace, Z. Upton, and N. H. Voelcker. "Sensors and imaging for wound healing: a review". In: *Biosensors and Bioelectronics* 41 (2013), pp. 30–42. ISSN: 0956-5663.

[71] Y. Hattori, L. Falgout, W. Lee, S. Jung, E. Poon, J. W. Lee, I. Na, A. Geisler, D. Sadhwani, and Y. Zhang. "Multifunctional skin-like electronics for quantitative, clinical monitoring of cutaneous wound healing". In: *Advanced healthcare materials* 3.10 (2014), pp. 1597–1607. ISSN: 2192-2640.

[72] M. S. Brown, B. Ashley, and A. Koh. "Wearable technology for chronic wound monitoring: current dressings, advancements, and future prospects". In: *Frontiers in bioengineering and biotechnology* 6 (2018), p. 47. ISSN: 2296-4185.

[73] C. Chen, Q. Xie, D. Yang, H. Xiao, Y. Fu, Y. Tan, and S. Yao. "Recent advances in electrochemical glucose biosensors: a review". In: *Rsc Advances* 3.14 (2013), pp. 4473–4491.

[74] M. Tsuneyasu, C. Sasakawa, N. Naruishi, Y. Tanaka, Y. Yoshida, and K. Tawa. "Sensitive detection of interleukin-6 on a plasmonic chip by grating-coupled surface-plasmon-field-enhanced fluorescence imaging". In: *Japanese Journal of Applied Physics* 53.6S (2014), 06JL05. ISSN: 1347-4065.

[75] K. Rathee, V. Dhull, R. Dhull, and S. Singh. "Biosensors based on electrochemical lactate detection: A comprehensive review". In: *Biochemistry and Biophysics Reports* 5 (2016), pp. 35–54. ISSN: 2405-5808.

[76] L. Santos, J. P. Neto, A. Crespo, D. Nunes, N. Costa, I. M. Fonseca, P. Barquinha, L. Pereira, J. Silva, and R. Martins. "WO3 nanoparticle-based conformable pH sensor". In: *ACS applied materials & interfaces* 6.15 (2014), pp. 12226–12234. ISSN: 1944-8244.

[77] J. Luo, T. Dziubla, and R. Eitel. "A low temperature co-fired ceramic based microfluidic Clark-type oxygen sensor for real-time oxygen sensing". In: *Sensors and Actuators B: Chemical* 240 (2017), pp. 392–397. ISSN: 0925-4005.

[78] P. Salvo, F. Di Francesco, D. Costanzo, C. Ferrari, M. G. Trivella, and D. De Rossi. "A wearable sensor for measuring sweat rate". In: *IEEE Sensors Journal* 10.10 (2010), pp. 1557–1558. ISSN: 1530-437X.

[79] C. Wang, X. Yan, M. Smith, K. Kochhar, M. Rubin, S. M. Warren, J. Wrobel, and H. Lee. "A unified framework for automatic wound segmentation and analysis with deep convolutional neural networks". In: *2015 37th annual international conference of the ieee engineering in medicine and biology society (EMBC)*. IEEE, 2015, pp. 2415–2418. ISBN: 1424492718.

[80] D. P. Yadav, A. Sharma, M. Singh, and A. Goyal. "Feature extraction based machine learning for human burn diagnosis from burn images". In: *IEEE Journal of Translational Engineering in Health and Medicine* 7 (2019), pp. 1–7. ISSN: 2168-2372.

[81] B. Acha, C. Serrano, I. Fondón, and T. Gómez-Cía. "Burn depth analysis using multidimensional scaling applied to psychophysical experiment data". In: *IEEE Transactions on Medical Imaging* 32.6 (2013), pp. 1111–1120. ISSN: 0278-0062.

[82] M. Goyal, N. D. Reeves, A. K. Davison, S. Rajbhandari, J. Spragg, and M. H. Yap. "Dfunet: Convolutional neural networks for diabetic foot ulcer classification". In: *IEEE Transactions on Emerging Topics in Computational Intelligence* (2018). ISSN: 2471-285X.

[83] E. Alpaydin. *Introduction to machine learning*. MIT press, 2020. ISBN: 0262043793.

[84] G. E. Hinton, T. J. Sejnowski, and T. A. Poggio. *Unsupervised learning: foundations of neural computation*. MIT press, 1999. ISBN: 026258168X.

[85] L. P. Kaelbling, M. L. Littman, and A. W. Moore. "Reinforcement learning: A survey". In: *Journal of artificial intelligence research* 4 (1996), pp. 237–285. ISSN: 1076-9757.

[86] C. Kingsford and S. L. Salzberg. "What are decision trees?" In: *Nature biotechnology* 26.9 (2008), pp. 1011–1013. ISSN: 1546-1696.

[87] I. G. Maglogiannis. *Emerging artificial intelligence applications in computer engineering: real word ai systems with applications in ehealth, hci, information retrieval and pervasive technologies*. Vol. 160. Ios Press, 2007. ISBN: 1586037803.

[88] V. S. Prasatha, H. A. A. Alfeilate, A. B. Hassanate, O. Lasassmehe, A. S. Tarawnehf, M. B. Alhasanatg, and H. S. E. Salmane. "Effects of distance measure choice on knn classifier performance-a review". In: *arXiv preprint arXiv:1708.04321* (2017).

[89] A. Tharwat, T. Gaber, A. Ibrahim, and A. E. Hassanien. "Linear discriminant analysis: A detailed tutorial". In: *AI communications* 30.2 (2017), pp. 169–190. ISSN: 0921-7126.

[90] L. F. S. Siqueira, R. F. A. Júnior, A. A. de Araújo, C. L. M. Morais, and K. M. G. Lima. "LDA vs. QDA for FT-MIR prostate cancer tissue classification". In: *Chemometrics and Intelligent Laboratory Systems* 162 (2017), pp. 123–129. ISSN: 0169-7439.

[91] S. Dreiseitl and L. Ohno-Machado. "Logistic regression and artificial neural network classification models: a methodology review". In: *Journal of biomedical informatics* 35.5-6 (2002), pp. 352–359. ISSN: 1532-0464.

[92] S. Huang, N. Cai, P. P. Pacheco, S. Narrandes, Y. Wang, and W. Xu. "Applications of support vector machine (SVM) learning in cancer genomics". In: *Cancer Genomics-Proteomics* 15.1 (2018), pp. 41–51. ISSN: 1109-6535.

[93] H. Bhavsar and M. H. Panchal. "A review on support vector machine for data classification". In: *International Journal of Advanced Research in Computer Engineering & Technology* 1.10 (2012).

[94] C. Gershenson. "Artificial neural networks for beginners". In: *arXiv preprint cs/0308031* (2003).

[95] A. Abraham. "Artificial neural networks". In: *Handbook of measuring system design* (2005).

[96] R. Miotto, F. Wang, S. Wang, X. Jiang, and J. T. Dudley. "Deep learning for healthcare: review, opportunities and challenges". In: *Briefings in bioinformatics* 19.6 (2018), pp. 1236–1246. ISSN: 1467-5463.

[97] S. Haykin. *Neural networks: a comprehensive foundation*. Prentice-Hall, Inc., 2007. ISBN: 0131471392.

[98] Q. Ke, J. Liu, M. Bennamoun, S. An, F. Sohel, and F. Boussaid. "Computer vision for human–machine interaction". In: *Computer Vision for Assistive Healthcare*. Elsevier, 2018, pp. 127–145.

[99] W. Rawat and Z. Wang. "Deep convolutional neural networks for image classification: A comprehensive review". In: *Neural computation* 29.9 (2017), pp. 2352–2449. ISSN: 0899-7667.

[100] C. M. Bishop. *Pattern recognition and machine learning*. springer, 2006.

[101] D. P. Kingma and J. Ba. "Adam: A method for stochastic optimization". In: *arXiv preprint arXiv:1412.6980* (2014).

[102] M. Dash and H. Liu. "Feature selection for classification". In: *Intelligent data analysis* 1.3 (1997), pp. 131–156. ISSN: 1088-467X.

[103] J. Tang, S. Alelyani, and H. Liu. "Feature selection for classification: A review". In: *Data classification: Algorithms and applications* (2014), p. 37.

[104] P. E. McKight and J. Najab. "Kruskal-wallis test". In: *The corsini encyclopedia of psychology* (2010), p. 1.

[105] G. Chandrashekar and F. Sahin. "A survey on feature selection methods". In: *Computers & Electrical Engineering* 40.1 (2014), pp. 16–28. ISSN: 0045-7906.

[106] H. R. Al Ghayab, Y. Li, S. Abdulla, M. Diykh, and X. Wan. "Classification of epileptic EEG signals based on simple random sampling and sequential feature selection". In: *Brain informatics* 3.2 (2016), pp. 85–91. ISSN: 2198-4018.

[107] W. Yang, K. Wang, and W. Zuo. "Neighborhood Component Feature Selection for High-Dimensional Data." In: *JCP* 7.1 (2012), pp. 161–168.

[108] M. W. Browne. "Cross-validation methods". In: *Journal of mathematical psychology* 44.1 (2000), pp. 108–132. ISSN: 0022-2496.

[109] A Primer, C. S. Burrus, and R. A. Gopinath. "Introduction to wavelets and wavelet transforms". In: *Proc. of International Conf.* 1998.

[110] A Rihaczek. "Signal energy distribution in time and frequency". In: *IEEE Transactions on information Theory* 14.3 (1968), pp. 369–374. ISSN: 0018-9448.

[111] D Abásolo, R Hornero, P Espino, D Álvarez, and J Poza. "Entropy analysis of the EEG background activity in Alzheimer's disease patients". In: *Physiological Measurement* 27.3 (2006), pp. 241–253. ISSN: 0967-3334. DOI: 10.1088/0967-3334/27/3/003.

APPENDIX A

Experimental plan for 3D skin model cultivation

General Instructions

Handle Phenion®FT Skin Models under sterile conditions only. It is recommended to use for the manipulation and cultivation, a laminar flow hood and an incubator for eukaryotic cell cultures (37° C, 5% CO2, at saturated humidity. Upon arrival, remove the tissues immediately from the semi-solid transport medium according to the guidelines below. Please follow the instructions, for the cultivation of the tissue in the Air-Liquid-Interface (ALI) up to 9 days. Please note, a longer cultivation might be possible but will ultimately lead to a Stratum corneum with aspects of hyperkeratosis.

Precautions / recommendations:

- Perform all steps under sterile conditions (respective lab trainings might be recommended).
- It is recommended to use exclusively the accessories (e.g. ALI-medium, filter and filter spacers, etc.), provided with the kit in order to ensure best cultivation conditions.

A) Culture of individual skin models separately

Experimental plan

1. Place three small petri dishes in one large petri dish and insert one filter spacer into each small petri dish ensuring correct position of filter spacer with **pin orientation upwards!**
2. Add 5ml of 37 ºC pre-warmed ALI-Medium into each small petri dish. The medium shall reach the upper tip of the filter spacer pins.
3. Carefully place small sterile filter papers on top of the spacer units to enable wetting of the filter with ALI-Medium.

Caution: After filters are soaked adjust level of ALI-Medium to ensure intense contact between the liquid phase and filter. The ALI-Medium and filter surface shall be on the same level, while the filter must not be over-flooded.

B) Set-up of Air Liquid Interphase culture system

1. Carefully open the protective cover and sealing of the 24-well plate containing the skin models. Remove the shipping protectors with forceps, granting free access to the full thickness skin models.

2. Very carefully grab the Phenion®FT Skin models using sterile forceps and transfer them on top of the filter papers. Make sure to avoid any air-bubbles between the tissue and the filter paper. Place one skin model per small petri dish or up to six skin models for the large petri dish.

3. After transferring the tissues, check that the filter papers are completely soaked with ALI-Medium. Avoid any air bubbles beneath the filter papers and the tissues. If needed, do not hesitate to add a little of ALI-Medium, ensuring that the basis of the Phenion®FT Skin Models on the filter paper in slight surrounded by the liquid.

4. After the final check, cover the tissue culture systems with the lid of the large petri dish and transfer them to the incubator for eukaryotic cell cultures.

5. For further cultivation (up to nine days) of the Phenion®FT Skin Models, ALI-Medium shall be changed every second day. For standard cultivations, there is no need for ALI-Medium changes at weekends.

APPENDIX B

Wavelet Families

Table B.1: Different wavelets family and their wavelets used during this work.

Wavelet Family	Wavelets
Haar	haar,
Daubechies	db2, db3, db4, db5, db6, db7, db8, db9, db10
Coiflet	coif1, coif2, coif3, coif4, coif5
Symlet	sym2, sym3, sym3, sym5, sym6, sym7, sym8
Fejer-Korovkin	fk4, fk6, fk8, fk14, fk22
Meyer	dmey
Biorthogonal	bior1.3, bior1.5, bior2.2, bior2.4, bior2.6, bior2.8, bior3.1, bior3.3, bior3.5, bior3.7, bior3.9, bior4.4, bior5.5, bior6.8
Reverse biorthogonal	rbio1.1, rbio1.3, rbio1.5, rbio2.2, rbio2.4 rbio2.6, rbio2.8, rbio3.1, rbio3.3, rbio3.5, rbio3.7, rbio3.9, rbio4.4, rbio5.5, rbio6.8

APPENDIX C

Experimental plan for 3D skin model cultivation

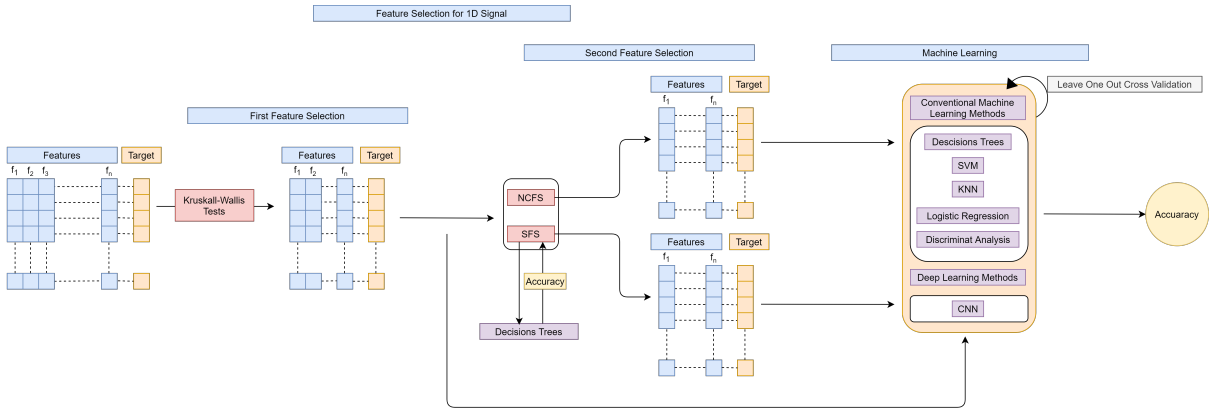

Figure C.1: Feature selection and machine learning algorithm methodology for 1D signals without the z-score normalization.

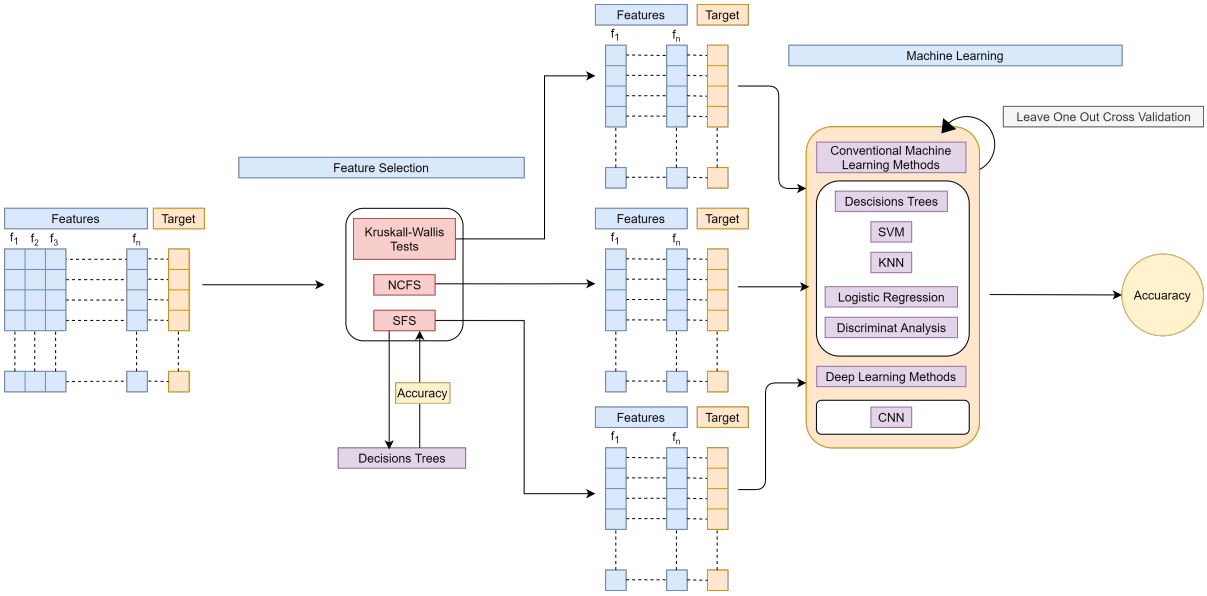

Figure C.2: Feature selection and machine learning algorithm methodology for 2D signals without the z-score normalization.

APPENDIX D

Accuracies of all the Machine Learning algorithms

Table D.1: Accuracy of the traditional machine learning algorithms using humidity features.

Machine Learning Algorithm	Feature Selection		Accuracy without z-score step (%)	Accuracy with z-score step (%)
	without z-score	with z-score		
Fine Tree	SFS	NCFS	58.9	62.5
Medium Tree	SFS	NCFS	58.9	62.5
Coarse Tree	SFS	NCFS	60.7	71.4
LD	SFS	SFS	64.3	66.1
LR	SFS	NCFS	64.3	69.6
Linear SVM	SFS	NCFS	66.1	67.9
Quadratic SVM	Kruskal - Wallis	SFS	67.9	69.6
Cubic SVM	SFS	SFS	57.1	62.5
Fine Gaussian SVM	SFS	NCFS	64.3	75.0
Medium Gaussian SVM	Kruskal-Wallis	NCFS	69.6	67.9
Coarse Gaussian SVM	SFS	SFS	64.3	60.7
Fine KNN	NCFS	NCFS/SFS	69.6	53.6
Medium KNN	SFS	NCFS	67.9	75.0
Cosine KNN	SFS/NCFS	SFS	62.5	60.7
Cubic KNN	SFS	NCFS	71.4	75.0
Weighted KNN	SFS	Kruskal-Wallis~	64.3	62.5

Table D.2: Accuracy of the traditional machine learning algorithms using temperature features.

Machine Learning Algorithm	**Feature selection**		**Accuracy without z-score step (%)**	**Accuracy with z-score step(%)**
	without z-score	**with z-score**		
Fine Tree	SFS	SFS	80.4	80.4
Medium Tree	SFS	SFS	80.4	80.4
Coarse Tree	SFS	SFS	80.4	80.4
LD	Kruskal - Wallis	SFS	76.8	82.1
LR	SFS	NCFS	71.4	80.4
Linear SVM	SFS	SFS	75.0	78.6
Quadratic SVM	SFS	SFS	78.6	76.8
Cubic SVM	SFS	NCFS	71.4	76.8
Fine Gaussian SVM	SFS	NCFS/SFS	78.6	71.4
Medium Gaussian SVM	SFS	NCFS	75.0	80.4
Coarse Gaussian SVM	NCFS	NCFS	60.7	83.9
Fine KNN	SFS	NCFS	78.6	75.0
Medium KNN	SFS	NCFS	71.4	82.1
Cosine KNN	SFS	NCFS/SFS	83.9	82.1
Cubic KNN	SFS	NCFS	76.8	82.1
Weighted KNN	SFS	NCFS	75.0	83.9

Table D.3: Accuracy of the traditional machine learning algorithms using a combination of humidity and temperature features.

Machine Learning Algorithm	**Feature selection (Humidity/Temperature)**		**Accuracy without z-score step (%)**	**Accuracy with z-score step(%)**
	without z-score	**with z-score**		
Fine Tree	SFS/SFS	SFS/SFS	80.4	76.8
Medium Tree	SFS/SFS	SFS/SFS	80.4	76.8
Coarse Tree	SFS/SFS	SFS/SFS	80.4	76.8
LD	SFS/SFS	NCFS/ NCFS	75.0	80.4
LR	NCFS/SFS	SFS/SFS	73.2	85.7
Linear SVM	SFS/SFS	NCFS/SFS	76.8	83.9
Quadratic SVM	SFS/SFS	SFS/SFS	80.4	82.1
Cubic SVM	NCFS/SFS	NCFS/ NCFS	78.6	80.4
Fine Gaussian SVM	SFS/SFS	NCFS/ NCFS	80.4	83.9
Medium Gaussian SVM	SFS/SFS	NCFS/ NCFS	76.8	85.0
Coarse Gaussian SVM	SFS/ Kruskal-Wallis	NCFS/ NCFS	71.4	83.9
Fine KNN	SFS/SFS	NCFS/ NCFS	76.8	80.4
Medium KNN	SFS/NCFS	SFS/SFS	75.0	76.9
Cosine KNN	SFS/SFS	NCFS/ NCFS	83.9	82.1
Cubic KNN	SFS/SFS	SFS/SFS	75.0	78.6
Weighted KNN	SFS/SFS	NCFS/ NCFS	76.8	82.1

Table D.4: Accuracy of the traditional machine learning algorithms using humidity and thermal image features.

Machine Learning Algorithm	**Feature Selection (Humidity/ Thermal Images)**		**Accuracy without z-score step (%)**	**Accuracy with z-score step(%)**
	without z-score	**with z-score**		
Fine Tree	SFS/SFS	SFS/SFS	70.8	72.9
Medium Tree	SFS/SFS	SFS/SFS	70.8	72.9
Coarse Tree	NCFS/SFS	SFS/SFS	70.8	72.9
LD	NCFS/SFS	NCFS/SFS	75.0	81.3
LR	Kruskal-Wallis/ SFS	NCFS/SFS	75.0	79.2
Linear SVM	NCFS/SFS	NCFS/SFS	83.3	81.3
Quadratic SVM	SFS/SFS	SFS/SFS	68.8	68.8
Cubic SVM	NCFS/ No FS used	Kruskal-Wallis/ NCFS	66.7	72.9
Fine Gaussian SVM	SFS/SFS	SFS/SFS	68.8	68.8
Medium Gaussian SVM	NCFS/SFS	NCFS/SFS	70.8	79.2
Coarse Gaussian SVM	NCFS/SFS	NCFS/SFS	77.1	77.1
Fine KNN	SFS/SFS	NCFS/ NCFS	72.9	75.0
Medium KNN	NCFS/SFS	SFS/SFS	79.2	72.9
Cosine KNN	SFS/SFS	NCFS/SFS	72.9	72.9
Cubic KNN	NCFS/SFS	NCFS/SFS	79.2	72.9
Weighted KNN	SFS/SFS	NCFS/SFS	75.0	72.9

Table D.5: Different CNN algorithms according to its performances.

SGD Algorithm	**Feature Selection**		**Accuracy without z-score step (%)**	**Accuracy with z-score step(%)**
	Withou z-score	**With z-score**		
Humidity Features				
sgdm	-	NCFS	-	75.0
RMSprop	SFS	SFS	57.1	66.1
adam	SFS	NCFS	59.0	73.2
Temperature Features				
sgdm	-	NCFS/SFS	-	78.6
RMSprop	SFS	NCFS	69.6	78.6
adam	SFS	SFS	76.8	76.8
Humidity + Temperature Features				
sgdm	-	NCFS /NCFS	-	85.7
RMSprop	SFS/SFS	NCFS/SFS	76.8	80.4
adam	SFS/SFS	NCFS/SFS	73.2	82.1
Humidity + Thermal images Features				
sgdm	Kruskal-Wallis/SFS	SFS/NCFS	72.9	72.9
RMSprop	SFS/SFS	SFS/SFS	66.7	72.9
adam	SFS/SFS	SFS/SFS	66.7	70.8

Table D.6: Performance of the thermal features from the 1^{st} data collection using traditional machine learning algorithms.

Machine Learning Algorithm	**z-score application**		**Accuracy without z-score step (%)**	**Accuracy with z-score step(%)**
	No	**Yes**		
Fine Tree	SFS	SFS	58.9	58.9
Medium Tree	SFS	SFS	58.9	58.9
Coarse Tree	SFS	SFS	64.3	66.1
LD	Kruskal-Wallis	Kruskal-Wallis	71.4	71.4
LR	NCFS	Kruskal-Wallis	73.2	71.4
Linear SVM	Kruskal-Wallis	SFS	64.3	66.1
Quadratic SVM	NCFS	NCFS/SFS	60.7	60.7
Cubic SVM	SFS	Kruskal-Wallis	67.9	64.3
Fine Gaussian SVM	NCFS/SFS	SFS	55.4	58.9
Medium Gaussian SVM	Kruskal-Wallis	SFS	62.5	66.1
Coarse Gaussian SVM	NCFS	SFS	64.3	66.1
Fine KNN	No FS used	No FS used	58.9	60.7
Medium KNN	Kruskal-Wallis	NCFS	62.5	67.1
Cosine KNN	Kruskal - Wallis	NCFS/SFS	62.5	60.7
Cubic KNN	Kruskal-Wallis	Kruskal-Wallis	60.7	62.5
Weighted KNN	No FS used	SFS	57.1	60.7

Table D.7: Performance of the thermal features from the 2^{nd} data collection using traditional machine learning algorithms.

Machine Learning Algorithm	**z-score application**		**Accuracy without z-score step (%)**	**Accuracy with z-score step(%)**
	No	**Yes**		
Fine Tree	SFS	SFS	71.2	80.3
Medium Tree	SFS	SFS	71.2	80.3
Coarse Tree	SFS	SFS	71.2	77.3
LD	Kruskal-Wallis/ NCFS	Kruskal-Wallis	72.7	75.8
LR	Kruskal-Wallis	Kruskal-Wallis	72.2	75.8
Linear SVM	NCFS	NCFS	71.2	71.2
Quadratic SVM	NCFS	NCFS	72.7	75.8
Cubic SVM	No FS used	No FS used	66.7	66.7
Fine Gaussian SVM	SFS	SFS	69.7	71.2
Medium Gaussian SVM	NCFS	Kruskal-Wallis	71.2	72.7
Coarse Gaussian SVM	NCFS	NCFS/SFS	71.2	71.2
Fine KNN	SFS	NCFS	68.2	69.7
Medium KNN	No FS used	Kruskal-Wallis	74.2	74.2
Cosine KNN	No FS used	No FS used	74.2	71.2
Cubic KNN	No FS used	No FS used	77.3	75.8
Weighted KNN	No FS used	No FS used	74.2	78.8

Table D.8: Performance of the thermal features from both the 1^{st} and 2^{nd} data collection using CNNs algorithms.

SGD Algorithm	**Feature Selection**		**Accuracy without z-score step (%)**	**Accuracy with z-score step(%)**
	Withou z-score	**With z-score**		
1^{st} Thermal Image Data Collection				
sgdm	Kruskal-Wallis	SFS	66.1	67.9
RMSprop	SFS	SFS	57.1	60.7
adam	Kruskal-Wallis/NCFS	SFS	53.6	67.9
2^{nd} Thermal Image Data Collection				
sgdm	Kruskal-Wallis/NCFS	No FS used	71.2	71.2
RMSprop	SFS	No FS used	72.7	71.2
adam	SFS	SFS	71.2	69.7